universität wien

http://physnano.univie.ac.at

DIPLOMARBEIT

Titel der Diplomarbeit

Mechanisms of Plastic Deformation in γ-Isotactic Polypropylene

angestrebter akademischer Grad

Magister der Naturwissenschaften (Mag.rer.nat)

Verfasser:	Gerald Polt
Matrikelnummer:	0503314
Studienrichtung (lt. Studienblatt):	Physik
Betreuer:	Ao. Univ.-Prof. Dr. Michael Zehetbauer

Wien, am 11. Februar 2011

Abstract

The γ-phase of isotactic polypropylene (iPP) shows an increased yield stress and elastic modulus compared to the α-phase of the same polymer. The arrangement of the chains in a non-parallel way in γ-iPP could be the reason for the higher resistance, in contrast to α-iPP where the chains are lined up in parallel. Another important question is whether crystallographic slip is still represented by dislocation motion as it is the case in α-iPP.

The main task of the present work was to clarify the question whether dislocations play a major role during plastic deformation in γ-iPP. For this purpose samples of γ-iPP were prepared by crystallization at elevated pressures using a specially designed pressure chamber being part of a universal testing machine. The γ-phase was subsequently investigated by special in-situ X-ray deformation experiments using synchrotron radiation revealing the existence of dislocations. Parameters such as the crystallinity, the dislocation density and the coherently scattering domain size (CSD-size) have been evaluated by means of the multireflection X-ray line profile analysis (MXPA) as a function of strain. The results are compared to the α-phase of the same polymer revealing an enhanced strength and a different development of the dislocation density in the γ-modified sample pointing at a different deformation mechanism. A model is presented explaining the development of the dislocation density in γ-iPP with respect to the CSD-size by formation of misfit dislocations.

Kurzfassung

Die γ-Phase von isotaktischem Polypropylen (iPP) zeigt im Gegensatz zur α-Phase desselben Polymertyps einen höheren Elastizitätsmodul und eine erhöhte Streckgrenze. Die Tatsache, dass die Ketten in γ-iPP nicht parallel angeordnet sind, wie dies in α-iPP der Fall ist, könnte die Ursache der erhöhten Festigkeit sein. Eine weitere wichtige Frage ist, ob das kristallographische Gleiten, ähnlich wie in α-iPP, durch eine Versetzungsbewegung hervorgerufen wird.
Die Hauptaufgabe dieser Arbeit war es zu klären, ob Versetzungen eine bedeutende Rolle während der plastischen Verformung in γ-iPP spielen. Zu diesem Zweck wurden mithilfe einer Druckkammer, welche an einer Universalprüfmaschine installiert ist, γ-iPP Proben unter erhöhtem Druck kristallisiert. Die γ-Phase wurde anschließend mittels speziellen in-situ Röntgendiffraktions- Deformationsexperimenten, und Synchrotron Strahlung untersucht wobei die Existenz von Versetzungen nachgewiesen wurde. Parameter wie Kristallinität, Versetzungsdichte und kohärent streuende Domänengröße wurden mittels der multireflection X-ray line profile analysis (MXPA) als Funktion der Dehnung ausgewertet. Die Resultate wurden mit denen von α-iPP verglichen, wobei sich eine erhöhte Festigkeit und eine unterschiedliche Entwicklung der Versetzungsdichte ergab, was auf einen andersartigen Verformungsmechanismus hindeutet. Ein einfaches Model wird präsentiert, welches die Entwicklung der Versetzungsdichte in γ-iPP im Verhältnis zur kohärent streuenden Domänengröße durch Bildung von misfit Versetzungen erklärt.

Contents

1. Introduction and Aim of Work

The behavior of semi-crystalline polymers under plastic deformation is of high interest and therefore subject of current research in polymer physics. It is controversially discussed if the plastic behavior is restricted to crystallographic processes and/or melting- and recrystallization. Recent investigations show that both mechanisms can occur depending on the deformation conditions [1]. In the case of crystallographic deformation, dislocations play a major role. In contrast to metals where dislocations are generated by a Frank-Read mechanism dislocations are thermally activated in polymers. The role of dislocations in semi-crystalline polymers was mainly studied by grown-in dislocations which are formed during the crystallization process, while mobile dislocations are generated by the deformation process itself. Wilhelm et al. [2] proved for the first time the existence of dislocations in α-iPP (isotactic Polypropylene) and further, that the amount of dislocations in α-iPP changes significantly under plastic deformation. An important tool for the evaluation was the Multireflection X-ray Profile Analysis (MXPA) which has already been applied successfully to various materials in metal physics [3, 4].
The choice fell on iPP because it contains different phases, namely the α- and the γ-phase, with different mechanical properties. Second, iPP contains sufficient peaks in the diffraction profile which is essential for applying the MXPA-Method, therefore i.e. PE (Polyethylene) can not be used. The γ-phase of iPP is characterized by enhanced mechanical properties caused by the unique crystallographic structure compared to usual polymers i.e. the α-phase of the same material.
The aim of this work was a detailed investigation of the γ-phase of iPP by means of the MXPA-Method and can be divided into three parts:

(i) Production of γ-samples

(ii) Mechanical characterization

(iii) Clarify the question whether dislocations are present and play a major role during plastic deformation in γ-iPP

ad(i) In order to produce samples with a high amount of γ-phase, high pressures and temperatures have to be applied. Therefore a pressure cell had to be built (see chapter 7) which was mounted at a universal testing machine of the type “Shimadzu AG50“. A ceramic heating tape which was located around the upper part of the pressure cell ensured the homogenous thermal

conditions necessary for crystallizing iPP in the γ-form.

ad(ii) In-situ X-ray deformation experiments have to be carried out on samples with a high amount of the γ-phase. By comparing the results to the α-phase of the same polymer one can investigate the differences in the mechanical properties such as strength.

The results were compared to the α-phase of the same polymer revealing an enhanced strength of the γ-phase.

ad(iii) To investigate the evolution of parameters such as the dislocation density and the crystallite size during plastic deformation, in-situ compression tests have to be performed at the Synchrotron light laboratory ELETTRA in Trieste, Italy. The use of synchrotron radiation during the in-situ deformation experiment is essential since a very high signal-to-noise ratio is mandatory for the application of the MXPA-Method in which as many diffraction orders as possible need to be recorded. Another point is that the samples become thicker with increasing deformation which in turn requires a high intensity for measuring in a transmission setup. Since the structural relaxation of a polymer material is quite fast at room temperature, synchrotron radiation is necessary to keep the measuring times at a minimum.

2. Theory

2.1 Morphology

Polymer materials consist of macromolecular organic connections built from covalent bonded repeating monomer units. Substituents are attached to the main chain of the linear macromolecule and have a different structure compared to the backbone. These substituents are atoms or groups of atoms i.e. benzol rings, which are replaced by another atom of the macromolecule. Since the substituents can be located on one or the other side of the main chain we have to distinguish between different types of tacticity.

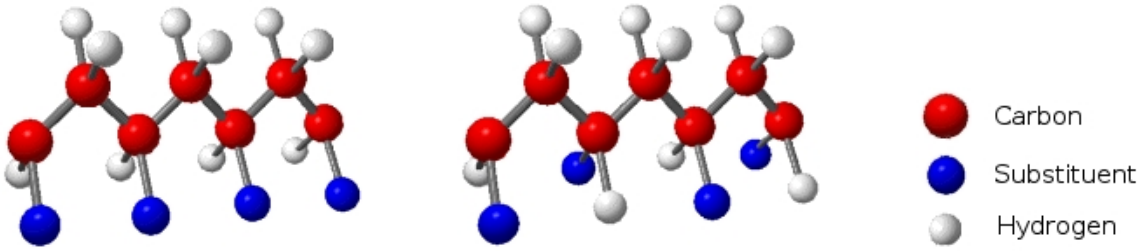

(a) isotactic **(b)** syndiotactic **(c)**

Figure 2.1: Isotactic and syndiotactic arrangement of the substituents on the main chain [5]

Figure 2.1a represents an isotactic arrangement, i.e. all substituents are located on the same side of the macromolecular chain. If the arrangement of the substituents is alternating (figure 2.1b) on one and on the other side it is known as a syndiotactic chain arrangement. Statistically irregular located substituents are assigned to the atactic structure. The reason why an isotactic Polypropylene was used is the following: The more regular the arrangement of the substituents, the higher is the possibility that the macromolecules arrange themselves in a close-packed parallel manner and therefore crystals can form more easily [6].

When the surface of a polymer is observed by a polarized optical microscope, one can find the so called spherulithic structure (figure 2.2). Spherulites are centralsymmetric superstructures and consist of crystalline lamellae starting to nucleate on a seed which can be for example dust. The growth starts at the center and spreads readily in all directions to the outside. They are formed when a thermoplastic polymer is cooled down from the melt, and can reach diameters from 0.1 to 1.0 mm. The size and the number of spherulites influences the mechanical properties

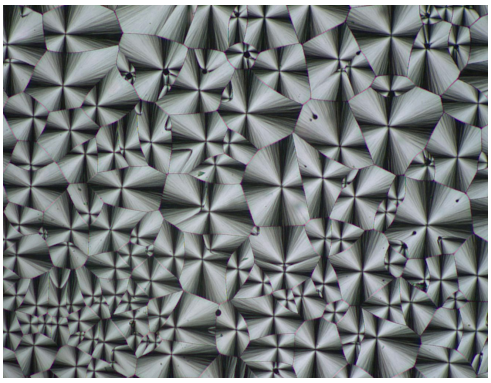

Figure 2.2: Spherulithic structure of a polymer observed by a polarized optical microscope [7]

and can be controlled by the cooling conditions from the melt. Cooling down slowly results in less spherulites, but they get bigger since they have more time to grow. When the melt is cooled down rapidly, the crystallization starts at various places simultaneously resulting in a higher amount of spherulites with smaller sizes (figure 2.3).

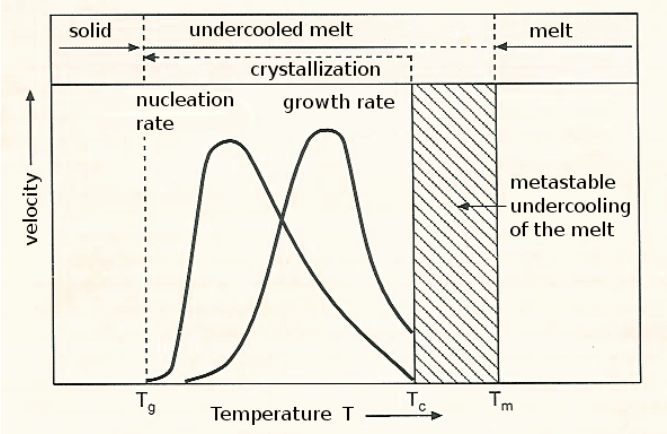

Figure 2.3: Temperature dependence of the nucleation- and growth rate when cooling down from the melt. T_g =glass-transition temperature, T_c =crystallization temperature, T_m =melting temperature [6]

Figure 2.4 shows the morphological structure of a usual polymer material. With dimension of about $10\mu m$ one can observe the spherulites build from the crystalline lamellae spreading from the center to the edge. The thickness of the lamellae is of the order of 25 nm in average, depending on the material. The amorphous phase being located between the lamellae and is characterized by a missing long range order. It is formed by the macromolecular chains exiting from a crystalline lamella, chains which leave one crystallite and enter into another one, so called "Tie Molecules", or chain loops. The crystallographic structure of the crystals is composed of unit cells with dimensions of 0.1 - 1 nm [8].

Isotactic Polypropylene crystallizes in three different morphological forms which can be distinguished by the arrangement of the macromolecular chains [10, 11]. The most common crystal

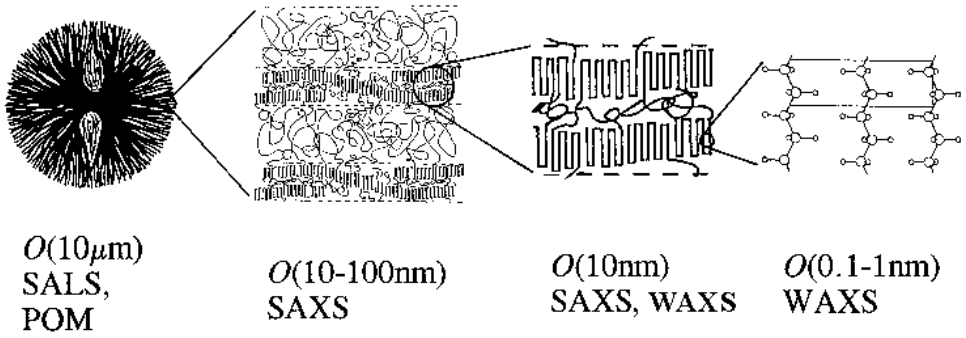

Figure 2.4: Principle structure and the characterization technique of a polymer material from left to right: Spherulites: small-angle light scattering (SALS); polarized optical microscope (POM), microdomains: small-angle X-ray scattering (SAXS), crystallites: (SAXS), unit cell: wide-angle X-ray scattering (WAXS) [9]

modification of iPP is the monoclinic α form, which is also the most stable form. Fig 2.5a shows the crystallographic structure of α-iPP represented by two unit cells strung together. One can see that the chains are aligned parallel to each other, held together by the relatively weak van der Waals bonds, compared to the strong covalent bondings acting between C-C and C-H [6]. Another morphological form is the hexagonal β-form. It can be achieved at very special crystallization conditions or by adding β nucleation agents [12].

The orthorhombic γ form of iPP, first recognized a few decades ago, is distinguished by a relatively unusual morphology compared to other semi-crystalline polymers (figure 2.5b). Its crystallographic structure was first identified to be of the triclinic form, but many X-ray diffraction experiments showed that this was wrong. Nowadays the γ-phase is identified as orthorhombic. The unique structure of this phase is expressed by the fact that the chain axes are not aligned in one direction. Instead, this structure contains sheets or bilayers composed of parallel helices. The bilayers are tiltet at an angle of approximately 80° against each other and about 50° with respect to the crystallographic a-axis [10, 11, 13]. According to figure 2.5b one can assume that the most probable slip plane may be between two molecular chains with the same orientation. A slip of two bilayers against each other seems unlikely due to an interlock of the methyl groups. Samples containing a high amount of γ-phase can be obtained by crystallizing an iPP homopolymer at high pressures. When moderate pressures are applied, crystallization in α and γ form occurs simultaneously. By increasing the pressure till 200 MPa, the γ phase becomes predominant, by exceeding 200 MPa crystallization exclusively occurs in the γ-phase [10].

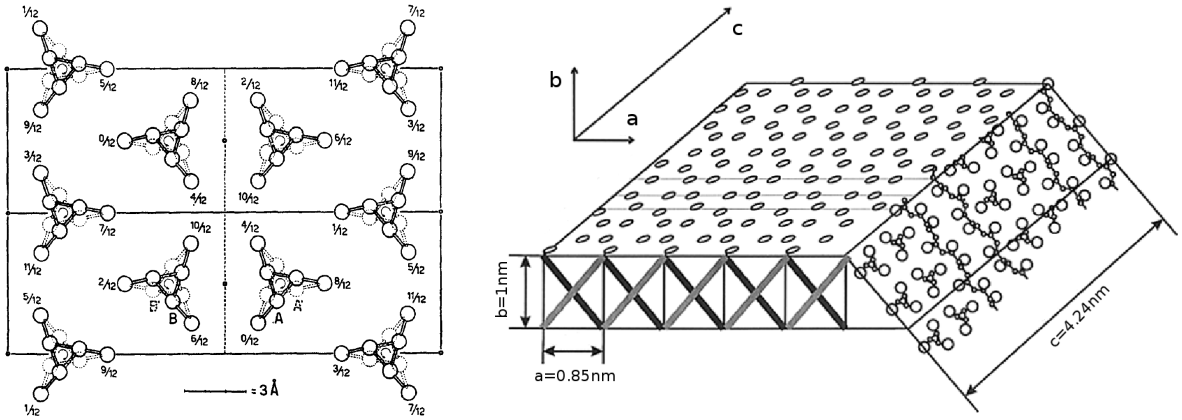

(a) α-iPP **(b)** γ-iPP

Figure 2.5: (a) Unit cell of α-iPP [10], (b) Unit cell of γ-iPP [14].

2.2 Crystallization of γ-Polypropylene

At atmospheric pressure, the γ-phase of isotactic Polypropylene is rarely observed in bulk samples. However, the crystallization in the γ-phase was observed (i) when crystallizing at elevated pressures [15, 13], (ii) using samples of very low molecular weight (1000 - 3000 g/mol) [16, 17], (iii) in random copolymers such as iPP [18, 19].
Figure 2.6 shows an X-ray diffraction profile of iPP samples with different content of the γ-phase. The amount of γ-phase can easily be estimated by using Equation 2.1 proposed by Turner and Jones [18] where $I_\gamma(117)$ and $I_\alpha(130)$ stands for the intensity of the (117) α- and (130) γ-peak, respectively. One can also use the area covered by each peak instead of the intensity. The most reliable result will of course be obtained by using all γ- and α-peaks.

$$K_\gamma = \frac{I_\gamma(117)}{I_\gamma(117) + I_\alpha(130)} \tag{2.1}$$

The required conditions for crystallizing in the γ-form can also be read from the phase diagram indicated in figure 2.7. According to Mezghani and Phillips [20] the crystal growth rate is too slow at low pressures (p<100MPa) so that a total crystallization of the sample in the γ-phase does not occur due to its degradation. Therefore a pressure of at least 200 MPa has to be applied under isothermal conditions (point A). Moreover, the sample has to be heated up above the melting temperature for a few minutes (point B) and then cooled down to the required crystallization temperature which is ideal for the corresponding material (point C). After about 4 hours the sample can be cooled down and removed from the pressure cell (point D). The diagram shows that crystallization in the γ-phase already occurs at a temperature of about 180 ℃, which is of course highly dependent on the used iPP type.

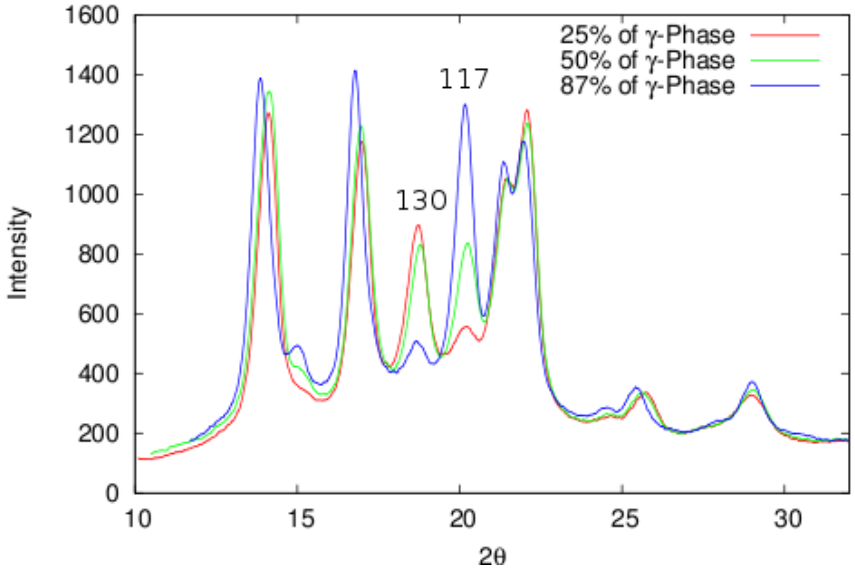

Figure 2.6: Diffraction profiles at different stages of deformation. The volume fraction of the γ-phase was determined by equation 2.1

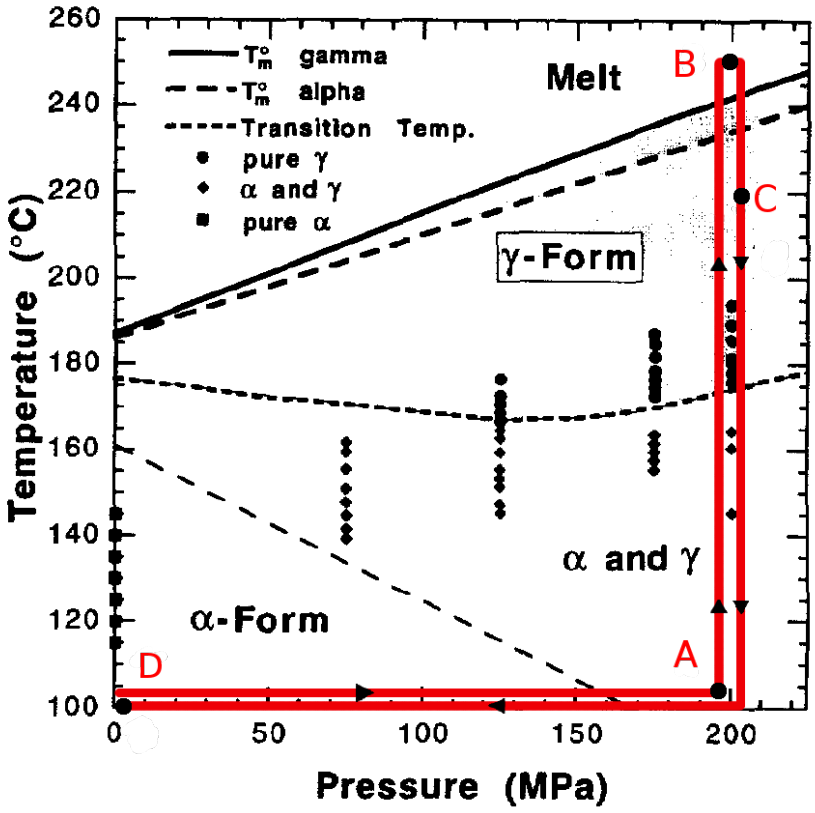

Figure 2.7: Phase diagram of iPP [20]

2.3 Crystal Defects

In this section the role of crystal defects such as dislocations shall be discussed using first the example of metals [21, 22]. The two basic types of dislocations are the edge- and the screw-dislocation. A bent dislocation line known as mixed dislocation, is continuously built from those two types of dislocations. The easiest way to imagine an edge dislocation is to consider a perfect crystal and insert an additional plane of atoms as indicated in figure 2.8. The boundary limit of this introduced plane represents the so-called dislocation line.
A screw dislocation is obtained if a perfect crystal is cut into two pieces and put together shifted by one or several atom positions in parallel to the cut [21]. If one draws a line perpendicular to the dislocation line around the screw dislocation it is not possible to get back to the starting point since one moves along a helix.
Every dislocation can be determined using its line element and its Burgers vector. The line element is defined as a tangential vector to the dislocation line. The value of the Burgers vector has to be determined as follows. If for example an edge dislocation is considered, a closed circuit has to be drawn around the core of the dislocation through the surrounding atoms which is known as the "Burgers-circuit". Now the same circulation has to be transferred into the undeformed lattice and one will see that the starting and the end point do not fit together. The distance which is necessary to connect these two points defines the Burgers vector $\vec{b}$.

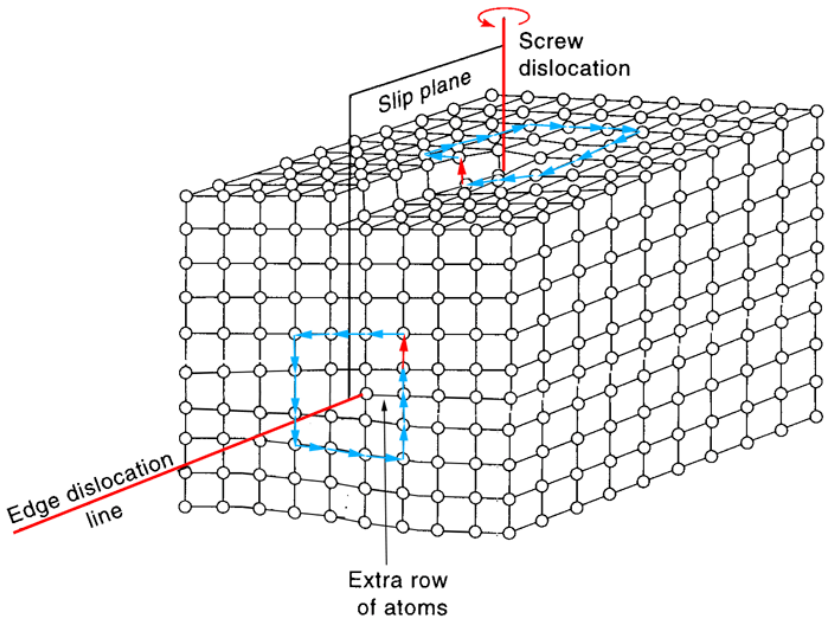

Figure 2.8: Schematic drawing of a screw- and edge dislocation in a crystal with its corresponding slip plane [23]

For edge dislocations the Burgers vector is perpendicular to the dislocation line, in the case of screw dislocations the Burgers vector is oriented in parallel to the dislocation line (see figure 2.8). Since the line element can change along the dislocation line but the Burgers vector does

not, the character of a dislocation can change from edge to screw character (figure 2.9).

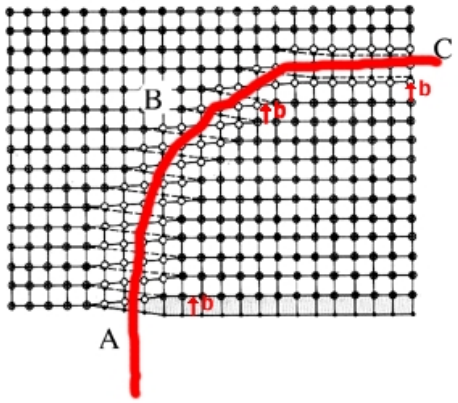

Figure 2.9: Mixed dislocation: (red line) The character of the dislocation changes from screw in A to edge in C [24]

In analogy to metals, the theoretical shear strength of a perfect polymer crystal is much higher than the measured one. The difference is caused by the presence and movement of dislocations through the crystal, resulting in smaller shear stress which has to be applied. This means if a certain CRSS (Critical Resolved Shear Stress) is reached within a slip system the two parts of the crystal are subjected to a relative movement against each other guided by a dislocation movement [8]. The favoured slip in polymer materials is the chain slip with the Burgers vector in chain direction as indicated in figure 2.11. In most polymers the transverse slip is more unlikely since a higher CRSS is needed to activate this kind of slip system, except in γ-iPP where chain slip is prohibited due to its non-parallel arrangement of the chains. A slip with shearing of the chains is impossible due to the strong covalent C-C bondings in the molecular chain. However, Shadrake and Guiu [25] performed minimum line-energy calculations to reveal the most possible types of dislocations in polyethylene. The results show that screw dislocations have generally lower line energies than edge-dislocations in which the screw dislocation in chain direction possesses the lowest line energy. This is therefore the most favoured slip in PE (figure 2.10d).
Figure 2.10 represents the four possible types of dislocations in polyethylene crystals. The deformation with the Burgers vector in parallel to the chains is called “chain slip”, with the Burgers vector perpendicular to them is called “transverse slip”.

2.4 Plasticity of the γ-Phase of Polypropylene

Plastic deformation is mainly guided by two different mechanisms. On the one hand there is the interlamellar movement within spherulites, but on the other hand there is intralamellar slip within a crystal itself which is accompanied by dislocation generating processes.
The intralamellar slip can further be divided into two subgroups, namely the fine slip and the

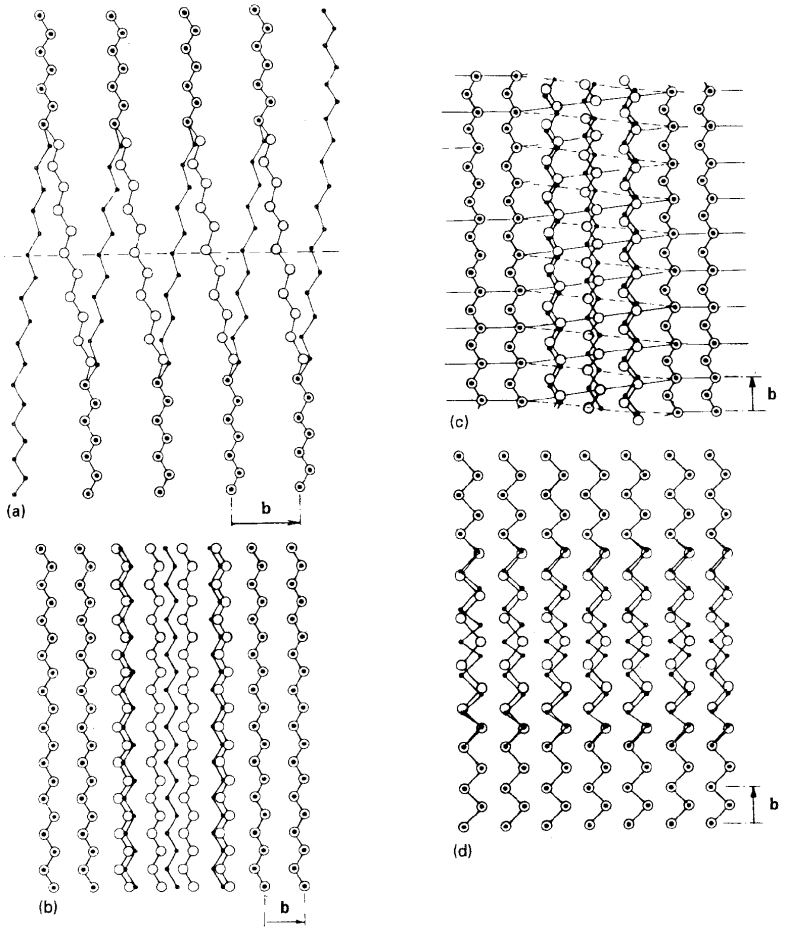

Figure 2.10: Models of dislocation in polyethylene: (a) screw dislocation with a Burgers vector normal to the chain, (b) edge dislocation with a Burgers vector normal to the chain, (c) screw dislocation with the Burgers vector in parallel to the chain (d) edge dislocation with a Burgers vector in parallel to the chain [8]

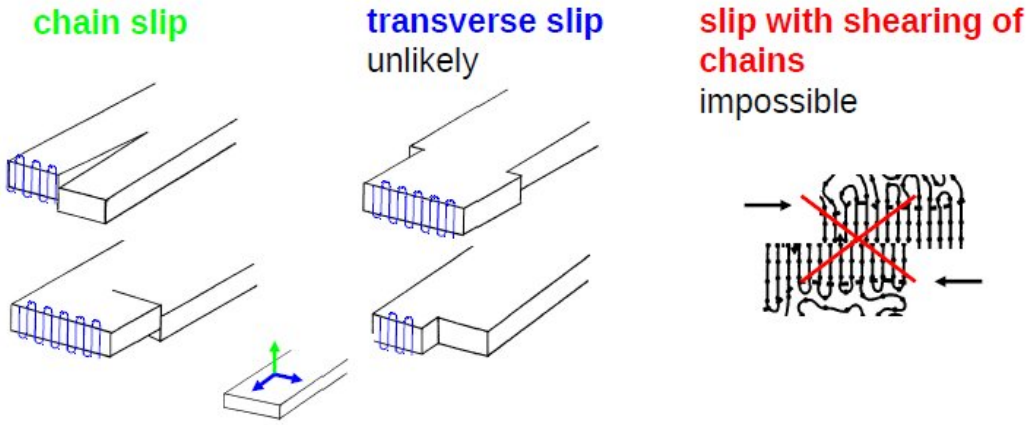

Figure 2.11: Slip systems in a semi crystalline polymer material

coarse slip [8] (figure 2.12). In the case of fine slip, a small amount of shear is applied to a large number of lattice planes resulting in a homogeneous deformation of the crystal and a deviation of the normal vector of the lamellae surface from the direction vector of the slip plane. In contrast to that, if a high amount of shear is applied on just a few parallel planes it is called "coarse slip". Hereby one can see a more or less inhomogeneous deformation of the lamellae not inducing a change in orientation of the normal vector of the lamellae surface and of the vector of the slip plane [8].
Figure 2.12c shows the shearing of a lattice with a large unit cell by fine slip. If the Burgers vector is less than the full translation vector of the unit cell, it is possible that deformation is caused by partial dislocations resulting in a change of the unit cell's shape. This intralamellar slip is reported as the main slip mechanism in most polymers undergoing a deformation process guided by a dislocation generating mechanism [8].

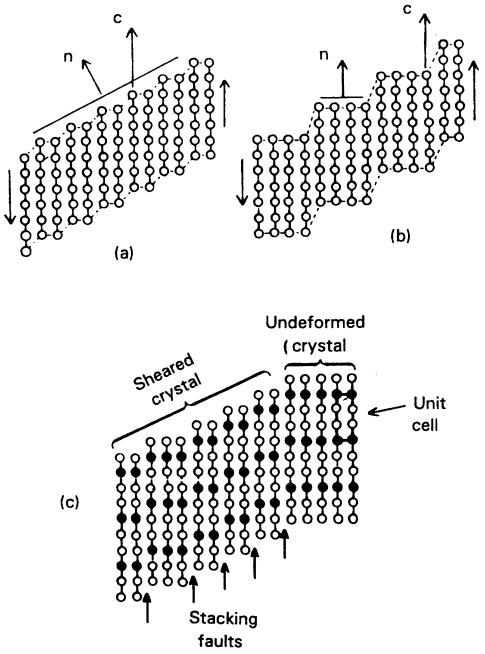

Figure 2.12: Intralamellar slip within a crystal [8]

In contrast to that, the interlamellar movement of lamellae within spherulites involves no shearing within the crystals under deformation. Also this type of slip can be divided into three subtypes depending on where the crystals are located in the spherulites. Figure 2.13 shows a sample undergoing a tensile test which results in a deformation of the spherulites in a way that its size changes from spherical to elliptic. The polar regions are defined as those regions towards which the tensile load is directed.

During tensile deformation the lamellae of the pole regions ⓐ start to shear against each other since they are aligned almost in parallel. The favoured slip in the lamellae themselves would be transverse slip due to the fact that the chain axes are oriented perpendicularly to the applied force. Here, deformation occurs first.

In the equatorial range ⓒ the lamellae are oriented perpendicularly to the tensile load. One can observe a separation of the lamellae in this region. Since the molecular chains are oriented in the direction of the tensile axis, the CRSS necessary for chain slip becomes very small. Therefore chain slip is the preferred slip mechanism in crystals located in this part of a spherulite.

The intermediate range ⓑ is characterized by a mixture of the two extreme regions. Here, crystal rotation can be observed, followed by chain slip and transverse slip as the predominant deformation modes within the lamellae.

It is important to mention that this type of plastic deformation, namely the interlamellar movement of the lamellae within the amorphous phase of the spherulites is considered to be the main slip mechanism in γ-isotactic Polypropylene. As already mentioned in Section 2.1 the γ-phase of iPP is characterized by a non-parallel chain nature. Hence there remains only one possible slip system which needs a much higher CRSS to be activated but, this has not been observed so far. Lezak et al. [13] suggested that the only allowed slip is the transverse slip in the (001) plane in the $< 010 >$ direction. It can therefore be concluded that if a certain amount of deformation is applied to a γ-iPP sample, no slip plane will be activated in a lamella but the lamellae will undergo an interlamellar movement. No dislocation generating process can take place. The dislocation density has to stay at a constant level with increasing deformation.

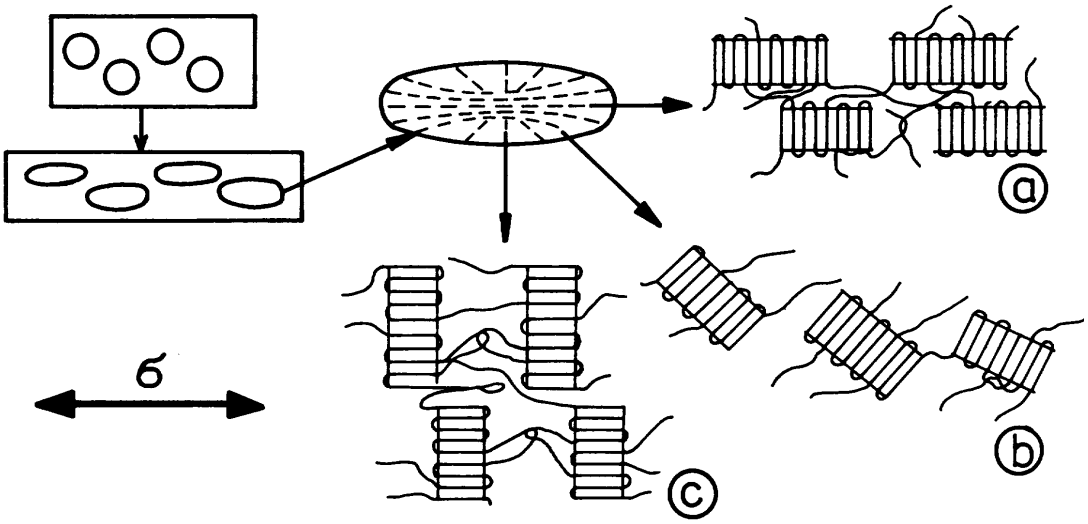

Figure 2.13: Interlamellar shear of crystalls within the amorphous phase [26]

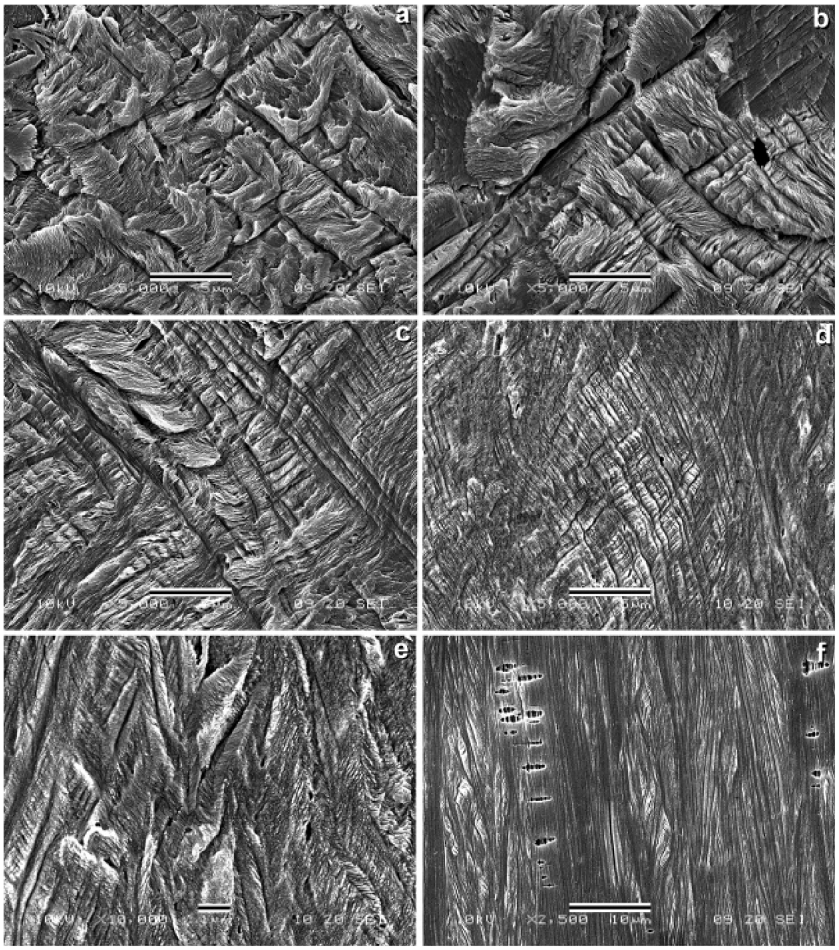

Figure 2.14: Development of shear bands with increasing strain. The plane of the image is the LD-FD plane with the loading direction horizontal. The sample was deformed to true strains of 0.07 (a), 0.18 (b), 0.41 (c), 0.71 (d,e), up to 0.93 (f) [13]

Figure 2.14 is an important requirement for the understanding of some results discussed in chapter 5 e.g. the development of the Coherently Scattering Domain -size (CSD) or crystallinity with increasing strain.

Figure 2.14 represents SEM (Scanning Electron Microscope) micro-graphs of a pure γ-sample deformed under plain strain compression performed by Lezak and Bartzak [13]. At early stages of deformation one can already observe a small formation of shear bands inclined by an angle of about 45° with respect to the loading direction. Further SEM studies showed that these shear-bands are created in the amorphous phase and start to spread over the sample cutting through the initial spherulithic structure. With increasing strain those shear bands multiply and propagate over the whole sample volume destroying the crystalline lamellae. They also begin to align towards the flow direction. The consequence of an increase in the shear band formation is that crystallinity decreases due to the deformation of the lamellae.

2.5 X-ray Line Profile Analysis

2.5.1 Generation of X-rays

The generation of X-rays in standard X-ray tubes is achieved by highly accelerated electrons impacting on a target material. First, a tungsten filament (cathode) is heated up by a current which starts to emit electrons under vacuum. These electrons are accelerated by a high voltage difference between the cathode and the target material (anode). A lot of heat is produced since the accelerated electrons have an energy of about 5 keV before they reach the target. This heat is removed by a water cooling mounted at the backside of the anode (figure 2.15).

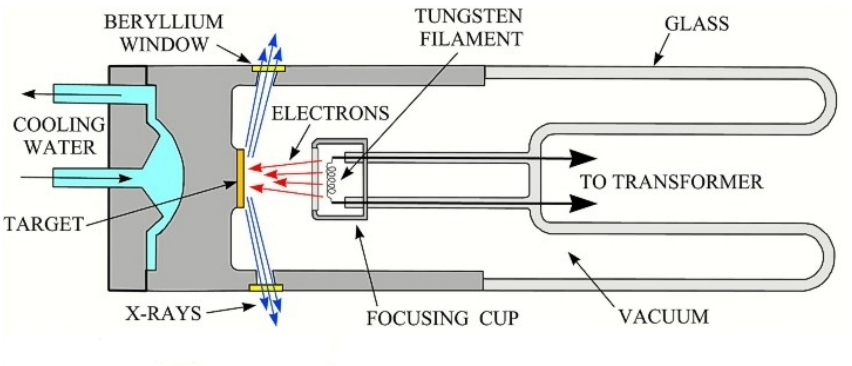

Figure 2.15: Schematic cross section of a X-ray tube [27]

The emitted electron which hits the target material, either copper or cobalt, ejects an electron from the K - shell of one of the atoms (figure 2.16b). An electron from a higher atomic shell fills up the vacancy in the K - shell, and simultaneously emits a X-ray photon is emitted. The energy of the emitted photon is equal to the energy difference between the two energy levels of the target atom. A K_α spectral line results from a L - shell to K - shell electron transition, a K_β spectral line from a M - shell to K - shell transition [28, 29].

To understand why there are just two spectral lines one has to take into account the so-called selection rules:

There are 2n-1 energy levels for each quantum number n.

$$l = 0, 1, 2, 3 \ldots n - 1 = s, p, d, f$$

$$j = l \pm \frac{1}{2}$$

The selection rules are as follows:

$$\Delta n = n_1 - n_2$$

$$\Delta l = \pm \frac{1}{2}$$

$$\Delta j = 0, \pm 1$$

Thus we get:

	n	l	j		
K	1	0	$\frac{1}{2}$	$1S\frac{1}{2}$	
L	2	0	$\frac{1}{2}$		
	2	1	$\frac{1}{2}$	$\alpha_2 \equiv 2P\frac{1}{2}$	occupied by $2 \cdot \frac{1}{2} + 1 = 2e^-$
	2	1	$\frac{3}{2}$	$\alpha_1 \equiv 2P\frac{3}{2}$	occupied by $2 \cdot \frac{3}{2} + 1 = 4e^-$
M	3	0	$\frac{1}{2}$		
	3	1	$\frac{1}{2}$	$\beta_2 \equiv 3P\frac{1}{2}$	
	3	1	$\frac{3}{2}$	$\beta_1 \equiv 3P\frac{3}{2}$	
	3	2	$\frac{3}{2}$		
	3	2	$\frac{5}{2}$		

Now it is obvious that the possibility for a $2P\frac{3}{2} \Longrightarrow 1S\frac{1}{2}$ transition is twice as high as for a $2P\frac{1}{2} \Longrightarrow 1S\frac{1}{2}$ transition, implying that:

$$I_{K_{\alpha_1}} : I_{K_{\alpha_2}} = 2 : 1$$

and due to a shielding by the L - shell:

$$(I_{K_{\alpha_1}} + I_{K_{\alpha_2}}) : I_{K_\beta} = 6 : 1$$

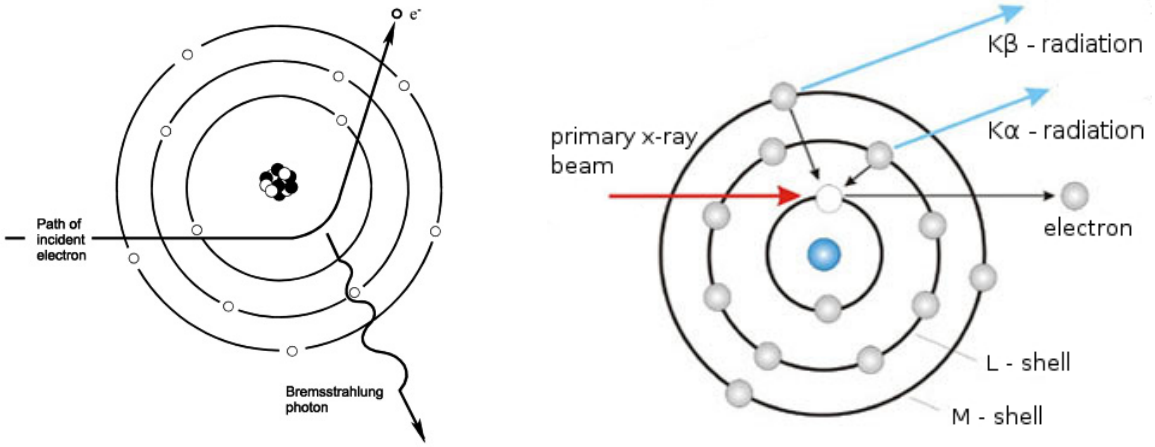

(a) Generation of the continuous spectrum by a slowed down electron in the electric field of an atom [30]

(b) An electron transition from the L- to K-shell results in K_α radiation, from the M- to K-shell in K_β radiation [31]

Figure 2.16: The generation of the "Bremsstrahlung" (a) and the K_α and K_β radiation (b)

The typical radiation spectrum is depicted in figure 2.17. The continuous spectrum or Bremsstrahlung is caused by a charged particle like an electron passing through an electric field of a nucleus of an atom (figure 2.16a). Thereby the particle gets slowed down resulting in an emission of a X-ray photon with a certain frequency, described by the Einstein Equation.
To get the characteristic radiation it is necessary to apply a tube voltage of at least five times the excitation potential in kV which is usually about 40 kV.
If only the K_α spectrum is needed, an absorption material which filters the K_β wavelength has to be used. In the case of copper radiation, a nickel filter with its absorption edge between the K_α and K_β lines is used, thus eliminating the K_β radiation.

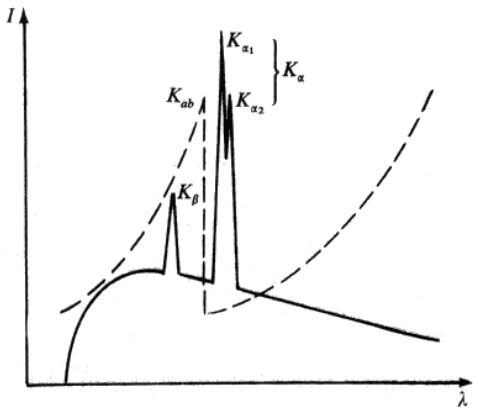

Figure 2.17: A typical radiation spectrum from a copper anode. The dashed line represents the absorption edge of the Ni-filter so that the K_β radiation is eliminated [32]

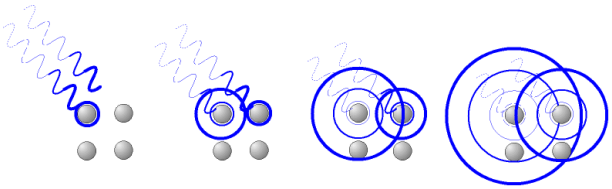

(a) X-ray radiation and its corresponding electromagnetic field excite the electrons of the atoms to vibrate. The vibrating electrons emit X-ray radiation as well which can be considered as waves of the corresponding atoms [33]

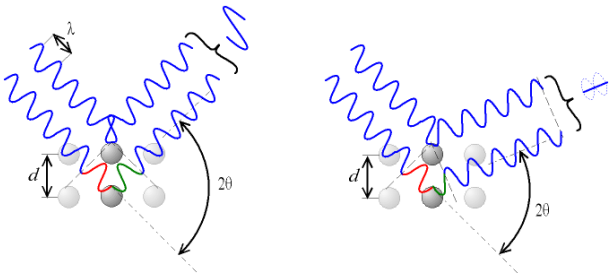

(b) When the X-ray radiation hits the sample at the right angle under a given lattice spacing and wavelength, constructive interference occurs [34]

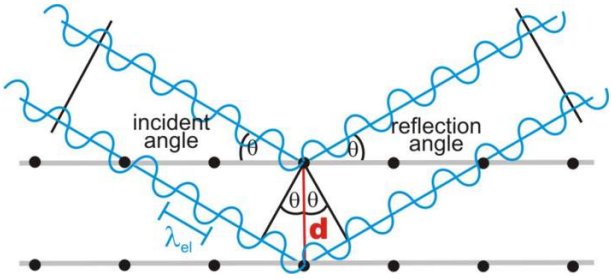

(c) Macroscopically it gives the impression as if the incoming X-ray radiation is reflected on the lattice plane [35]

Figure 2.18: The emitted waves of the electrons can be considered as waves of the corresponding atoms in first approximation (a), Constructive and destructive interference of reflected waves (b), Reflection of waves on a lattice plane (c)

2.5.2 X-ray Diffraction

Up to this point the generation of K_α radiation has been discussed, but what happens when the sample material is hit by a wave? X-ray radiation impinging on a crystal results in transmission on the one hand, making up the main part, but there is also a scattered radiation known as X-ray diffraction. The scattered waves result in a certain pattern on the detector or photo plate. The

lattice planes within a crystal act like semi-transparent mirrors reflecting the incoming waves, this phenomena is described by the Bragg's Law.

$$n\lambda = 2d \sin \Theta \tag{2.2}$$

$n \ldots$ order of diffraction

$\lambda \ldots$ wavelength

$d \ldots$ distance of the lattice planes

$\Theta \ldots$ angle between X-ray beam and lattice plane

If a X-ray beam with the wavelength λ impacts a lattice plane at an angle Θ with a lattice spacing d, reflection of the beam occurs. Only if the scattered radiation of parallel planes is in phase, reflected intensity can be observed, otherwise the Bragg equation is not fulfilled (figure 2.18b). If there is a phase difference between the diffracted beams, there will always be a second diffracted wave which extinguishes with the first due to the high amount of lattice planes.
Electrons of the atoms of the sample material are excited to vibrate by the incident X-ray radiation and its corresponding electromagnetic field. The vibrating electrons also start to emit X-ray radiation in the form of spherical waves (figure 2.18a) which add up to waves of the corresponding atoms in first approximation. Since the atomic distances in the crystal and the wavelength of the emitted X-ray radiation is of the same order of magnitude, interference occurs. If the Bragg-equation is fulfilled meaning that the X-ray radiation hits the crystal in the right angle constructive interference can be observed. Macroscopically this gives the impression that the waves are reflected by the crystal planes (figure 2.18c) [21, 28]. When these reflected waves hit a position sensitive X-ray detector they start to form a so called "X-ray line profile". The shape and the intensity of the line profile of course highly depends on the crystal lattice, wavelength, measurement time etc..

2.5.3 Modified Williamson-Hall Analysis

One of the methods which is used for evaluating the X-ray line profiles is the Williamson-Hall plot. The basic idea is that the FWHM (Full Width at Half Maximum) or the integral width are influenced by two main broadening effects namely, the crystallite-size being independent of the diffraction order, and the lattice distortion respectively, dependent of the diffraction order [36].

$$\Delta K_{FWHM} = 0.9/D + \alpha K \tag{2.3}$$

αK is the strain contribution to the peak broadening resulting from lattice distortions whereas D represents the crystallite domain size. By plotting the FWHM against the diffraction vector the broadening caused by the size and strain can be separated. However it turned out that

the evaluation is rather difficult due the anisotropy of the strain field. Figure 2.19a shows a Williamson-Hall plot of an iPP sample containing 88 ٪ of γ-phase. The strain anisotropy can be in some cases quantified by introducing the average contrast factor of dislocations $\overline{C}$ which leads to the modified Williamson–Hall plot as suggested by Ungár et al. [37]:

$$\begin{aligned} &\Delta K_{FWHM} = 0.9/D + \beta^{1/2} * \rho^{1/2} K\overline{C}^{1/2} + O(K^2\overline{C}) \\ &\text{with } \beta = \pi * M^2 b^2/2 \end{aligned} \tag{2.4}$$

$K \cdots$ absolute value of the diffraction vector

$D \cdots$ crystallite size

$b \cdots$ Burgers Vector

$M \cdots$ constant dependent on the outer cut-off-radius of dislocations

$\varrho \cdots$ average density of dislocations

$O \cdots$ higher order terms in $K^2\overline{C}$

$\overline{C} \cdots$ average contrast factor

With the modified Williamson–Hall plot, monotonous functions can be obtained by the use of the contrast factors of dislocations and allowing a more reliable separation of size and strain effects if the strain comes from dislocations. Therefore it is a reliable method to check if dislocations are present in a material i.e. in a melt crystallized polymer like the experiments of Wilhelm et.al. demonstrated [2]. By plotting the FWHM as a function of the diffraction vector multiplied by the square root of the average dislocation contrast factor($k\sqrt{\overline{C}}$) (figure 2.19) a monotonous curve is obtained if dislocations are present. While the interception of the extrapolated plot at $k = 0$ gives the inverse of the size, the slope of the line is proportional to the dislocation density.

2.5.4 Multiple Whole Profile Analysis using *CMWP-fit*

The Multiple Whole Profile Analysis (MWPA) uses ab-initio physical functions describing broadened peak profiles by size and strain effects. The peak profile is described by its Fourier Transformed A(L) which is, according to Warren and Averbach [39, 40]:

$$A(L) = A^S(L)A^D(L) \tag{2.5}$$

where L is the variable of the Fourier transform defined as $L = na_3$ where $a_3 = \frac{\lambda}{2}(sin\Theta_2 - sin\Theta_1)$, n are integers starting from zero, λ is the wavelength of the X-rays and $(\Theta_2 - \Theta_1)$ is the angular range of the measured diffraction profile. $A^S(L)$ and $A^D(L)$ are the size and distortion coefficients respectively.

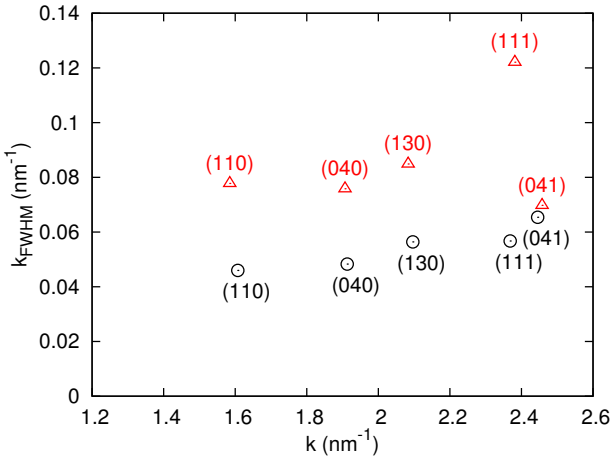

(a) The random arrangement of the data points is caused by an anisotropic strain field.

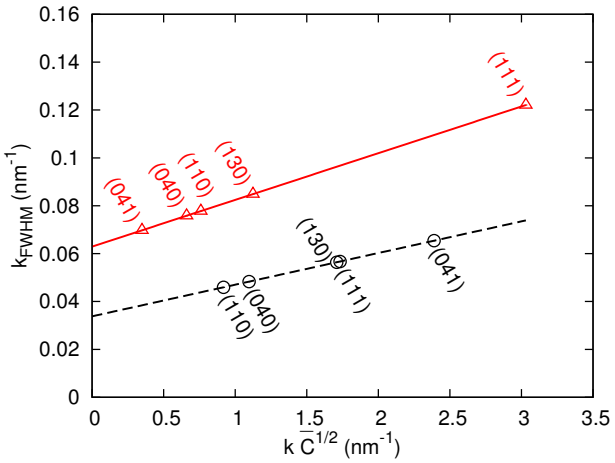

(b) The strain anisotropy can be corrected by introducing the average contrast factor of dislocations

Figure 2.19: Williamson Hall (a) and modified Williamson Hall plot (b) of α-iPP deformed to $\varepsilon = 0.5$ ($\triangle$) and before deformation ($\bigcirc$) [38]

Strain broadening

Warren and Averbach computed the strain broadening coefficient which is given by

$$A^D(L) = exp(-2\pi^2 g^2 L^2 \langle \varepsilon_L^2 \rangle) \tag{2.6}$$

where $\langle \varepsilon_L^2 \rangle$ is the mean square strain, g is the length of the diffraction vector. Several theoretical models have been developed describing the mean square strain in which Krivoglaz and Wilkens noticed that the major contribution of strain to peak broadening is caused by the strain

field of dislocations [41, 42].

$$\langle \varepsilon_L^2 \rangle = \left(\frac{b}{2\pi}\right)^2 \pi \varrho \; C f \left(\frac{L}{R_e}\right) \tag{2.7}$$

Here f is the Wilkens function depending on the effective outer cut off radius R_e. Among the Burgers vector b and the average dislocation density ϱ the dislocation contrast factor C is one of the main parameters of interest. The contrast factor determines the influence of the dislocations on the line profile, for example that if the Burgers vector b is perpendicular to the diffraction vector g (**bg=0**) dislocations have only a small or even no effect on the peak broadening.

While the dislocation contrast factor can be determined experimentally on the basis of the relative orientation of the diffraction vector g, the line vector l the Burgers vector b, and the elastic constants of the material for single crystals, only the average of the contrast factors can be observed in polycrystals. Ungár and Tichy [43] showed that under the assumption of equally occupied possible slip systems, or if the crystal shows only weak texture, the contrast factors of the hkl planes can be averaged over their permutations for different crystal structures resulting in $\overline{C}$, the average contrast factor.

By inserting Equation 2.7 in 2.6 the general distortion coefficient is obtained as:

$$A^D(L) = exp\left[-\left(\frac{\pi b^2}{2}\right)(g^2 C)\varrho \; L^2 f\left(\frac{L}{R_e}\right)\right] \tag{2.8}$$

Size broadening

For the computation of the peak profile more precisely its Fourier transform originating from a *spherical* crystallite, the crystal is divided into cylindrical columns perpendicular to the hkl diffraction planes or parallel to the diffraction vector g (figure 2.20).

The size intensity profile is obtained by the sum of the normalized integral intensity profiles of each crystal column with its area A_i and height M_i, which is of course dependent on the crystal shape and its size distribution.

In the case of *spherical crystals* and a lognormal size distribution, the size intensity function is as follows:

$$I^S(s) = \int_0^\infty M \frac{sin^2(M\pi s)}{(\pi s)^2} \; \text{erfc}\left[\frac{log\left(\frac{M}{m}\right)}{\sqrt{2\sigma}}\right] dM \tag{2.9}$$

with the complementary error function erfc, the variance σ and the median of the distribution m. By the use of Equation 2.9 its Fourier transformed $A^S(L)$ can be calculated but is not shown here due to its length (please see [44] for details).

Another possibility for calculating the Fourier transform is given by Guinier (1963):

$$A^S(L) = \frac{1}{V} \int \sigma(r)\sigma(r+L)d^3r \tag{2.10}$$

where $\sigma(r) = 1$ if r is within the scattering object, otherwise $\sigma(r) = 0$. Equation 2.10 shows that size broadening increases with decreasing scattering volume.

In the case of an *anisotropic crystal* represented e.g. by a spherical ellipsoidal shape (figure 2.20b) the size function depends on the hkl indices. The anisotropic size function is the same as in equation 2.9 with the only difference that the median m of the size distribution is depending on the reflection indices $m = m_{hkl}$.

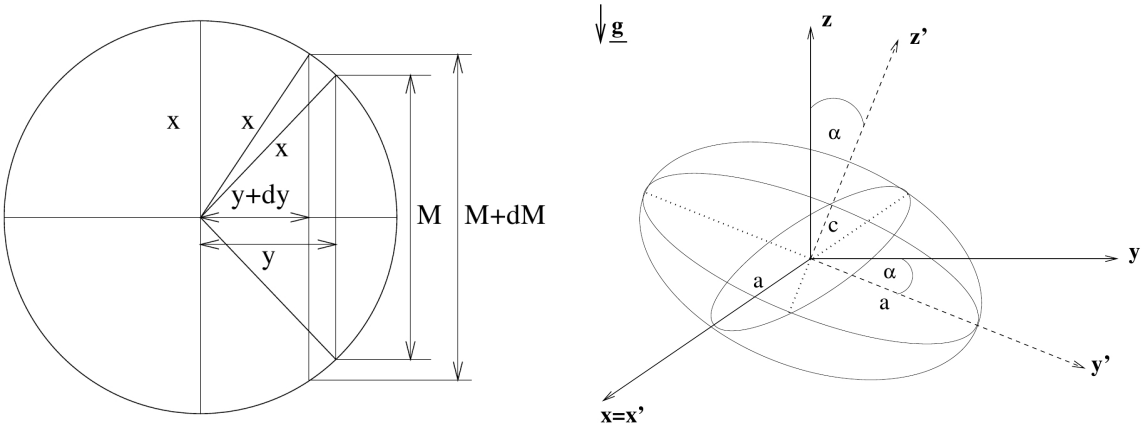

(a) Isotropic size broadening [45] **(b)** Anisotropic size broadening [45]

Figure 2.20: Size broadening

Coherently Scattering Domains (CSD)

Altogether, we can say that the evaluation of diffraction profiles by the MWPA-method is based on the model of size- and strain-broadening. While the strain broadening is caused by dislocations, the size-part of the peak broadening is determined by the Coherently Scattering Domain size (CSD-size) [46, 47, 45]. The CSD-size represents the *smallest* coherently scattering size in a crystal. Since the crystal shape can be either approximated by a cubic or cuboid geometry in polymers (figure 2.21), the smallest edge length can be related to the lamella thickness.

The ellipticity determines how far the geometric shape of a crystal differs from a cubic geometry, or even more precisely, the deviation of an ellipsoidal to a spherical function which is fitted into a crystallite. If a cubic crystal is considered, a spherical function is fitted into this shape (figure 2.21a) indicating that the ellipticity ε equals 1 ($\varepsilon = c/a$ according to figure 2.20b). In the case of a cuboid crystal (figure 2.21b) a rotational ellipsoidal function (spheroid) is used for the fitting

procedure. The ellipticity exceeds or falls below 1 depending whether the spheroid is oblate (lentil) or prolate (cigar) and increases in the absolute value, the higher the deviation of the fitted ellipse to a spherical shape is.

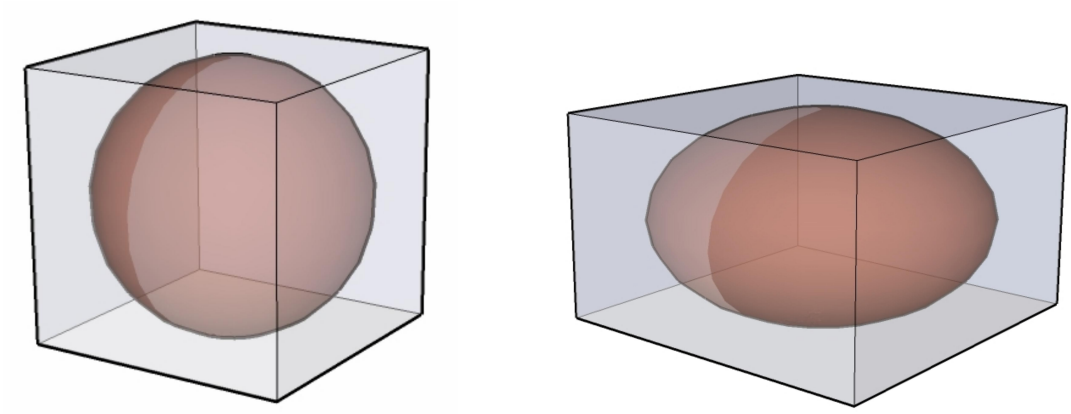

(a) A spherical function is fitted into a cubic crystal

(b) In the case of a cuboid crystal a spheroidal function (in this case an oblate spheroid) is used for the fitting.

Figure 2.21: Depending on the crystal shape whether a spherical (a) or spheroid (b) function is fitted. The greater the deviation from a sphere, the higher the value of the ellipticity ε.

CMWP-fit

The program used for the fitting procedure is "CMWP-fit" [44]. This program fits the whole intensity pattern of the measured diffraction profile by a background function and additional profile functions.

$$I_{theoretical} = BG(2\Theta) + \sum_{hkl} I^{hkl}_{MAX} I^{hkl}(2\Theta - 2\Theta^{hkl}_0) \tag{2.11}$$

where I^{hkl}_{MAX} is the peak intensity, $2\Theta^{hkl}_0$ is the 2Θ value at the peak center and I^{hkl} is defined as:

$$I^{hkl} = I^{hkl}_{\text{instrument}} \cdot I^{hkl}_{\text{size}} \cdot I^{hkl}_{\text{dislocations}} \cdot I^{hkl}_{\text{planar faults}} \tag{2.12}$$

with the instrumental profile $I^{hkl}_{\text{instrument}}$, and the theoretical profiles for size, strain and planar faults, I^{hkl}_{size}, $I^{hkl}_{\text{dislocations}}$, $I^{hkl}_{\text{planar faults}}$. The dependence of the theoretical profile functions from the microstructural parameters is shown in equation 2.8 and 2.9. It should be noted that the convolution of the profiles is carried out in the Fourier space and gets then transformed into real space by inverse Fourier transformation.

3. Experimental

The iPP used for crystallization was of the type HD120MO from "Borealis" (for more details see chapter 7) which was compression moulded to plates with dimensions of
120 x 80 x 10 mm. The first critical point was to ensure that no air intakes were caused during the processing. The plates have been cut with an ordinary saw into stripes with a width of about 10 mm and were milled off on a turning lathe to cylinders with a diameter of 8 mm. From these cylinders samples with the desired height have been cut by a "Struers Accutom-5" precision saw with a diamond blade under use of a slow feed rate to prohibit melting in the cutting area and to ensure that only little defects were introduced in the material.

3.1 Sample Preparation

3.1.1 Preparation of γ-iPP Samples - Pressure Cell

The crystallization procedure is explained by means of sample HD120MO_23. After a pressure of 200 MPa was applied the cell was heated up above the melting temperature T_m to about 255 ℃ (T_m =245 ℃ at p=200MPa [13]).

It is to mention that the temperatures given in table 3.1 may not be exactly the same as on the sample since the thermocouple is located in a certain distance to the specimen closer to the band heater. Especially for the first heating to the melting temperature there is a temperature gradient from the heating tape to the sample which disappears after equilibrium is reached. After holding the temperature for about 10 minutes above T_m it was reduced to the crystallization temperature T_c of 210 °C and held for 4 to 6 hours.
The pressure of at least 200 MPa was achieved by a pressure chamber (figure 3.1) mounted to a tensile testing machine of the type "Shimadzu AG50". The samples are located between a stamp out of tungsten carbide (part 10 in figure 3.1) and a piston surrounded by hardened steel (part 11) with high strength. After the hydrostatic pressure has been applied the sample is heated up above the melting temperature which is done by a band heater mounted around the casing (part 5) (figure 3.2) providing a heating rate of up to 13 °C/min due to the high power of 2000 Watt. The temperature is controlled by a "Eurotherm 3216N" PID temperature controller equipped with a sensor support for a Typ J thermocouple. The additional RS232 serial interface allows for a connection to a computer and therefore defining a desired temperature program. The cooling

from the melt to the crystallization temperature is done by two computer ventilators supplied by a 12 Volt power adapter. If the crystallization time is over, the pressure cell is cooled down using water flowing from the upper cooling fitting between the insert (part 6) and the casing (part 5) to the lower one. To unload, the drawer (part 18) with the pressure plate (part 16) is pulled out and the sample can be pressed out by the upper part of the stamp.

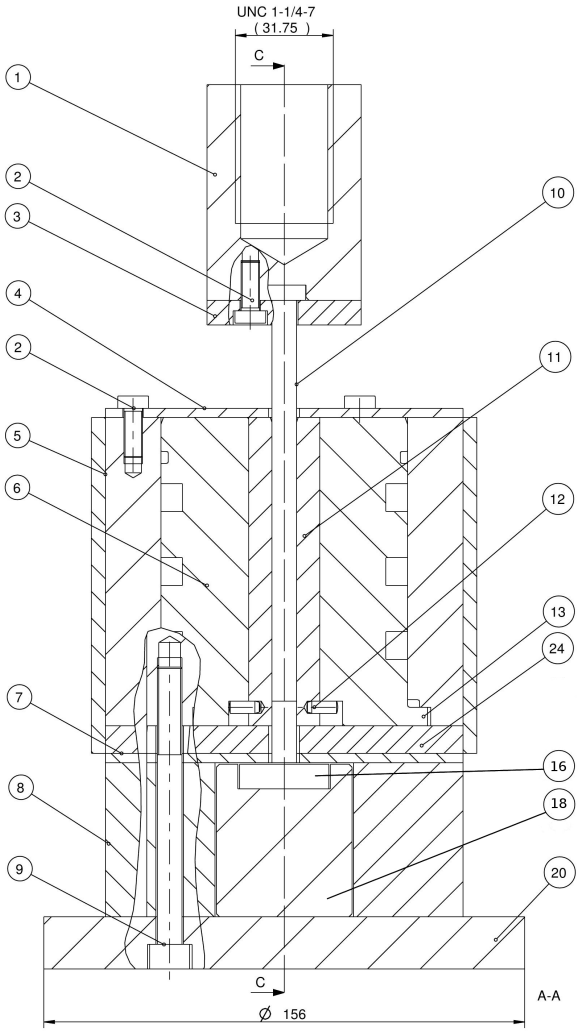

Figure 3.1: Pressure cell

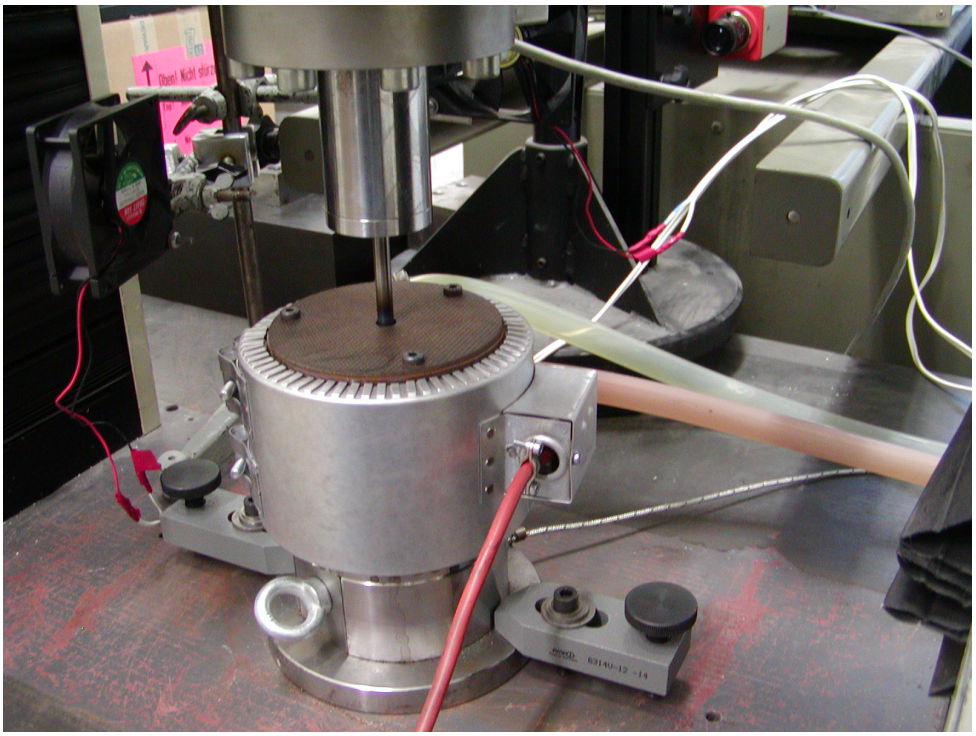

Figure 3.2: Pressure cell with band heater and ventilators for cooling mounted at the universal testing machine

3.1.2 Sample Overview

Table 3.1 shows an overview over the produced samples. At this point it has to be mentioned that the values of the γ-fraction may differ for the "BRUKER D8-GADDS" and the synchrotron measurements. The values for the γ-fraction of the samples HD120MO_1 and HD120MO_23 from table 3.1 are more reliable since they have been measured at the synchrotron facility. The reason for a difference is the following. The amount of γ-fraction was determined in the home lab using a "GADDS D-8" X-ray diffraction system measuring in reflection. It turned out that the γ-fraction estimated on the diffraction system and by synchrotron radiation differs significantly, since the γ-phase seems to be distributed inhomogeneously. By measuring in reflection only a small volume fraction of the sample is investigated whereas measuring in transmission like at the synchrotron allows to determine an average value of the fraction by the use of a bigger volume. The experiment has been performed with samples of different heights, but it can be assumed that the volume of the sample does not influence the crystallization behavior under the condition of a homogenous temperature distribution. Besides the pressure, crystallization temperature and experimental time are crucial parameters, because the longer the crystallization takes place, the more γ-phase can be achieved, since the molecular chains have more time to rearrange themselves. A higher crystallization temperature facilitates the movement of the chains but without sufficient undercooling, the thermodynamic requirements for crystallization can not be ensured.

Experiment	#	Date	Material	Pressure [Mpa]	Melting Temp Tm [°C]	Crystallization Temp Tc [°C]	Experiment Time [min]	Gamma Phase Content [%]	Sample Height [mm]
iPP_BE50_1	7	29/03/10	BE50	**200**	-	**198**	90	**15**	7
iPP_BE50_2	8	30/03/10	BE50	**200**	248	**200**	120	**25**	7
iPP_BE50_3	9	31/03/10	BE50	**239**	253	**205**	120	**20**	7
HD120MO_1	10	01/04/10	HD120MO	**200**	255	**200**	120	**40**	7
HD120MO_2	14	01/04/10	HD120MO	**200**	255	**200**	120	**38**	3
HD120MO_3	15	06/04/10	HD120MO	**200**	255	**190**	120	**22**	2
HD120MO_4	16	07/04/10	HD120MO	**200**	255	**200**	240	**88**	2
HD120MO_5a	-	-	HD120MO	**-**	-	**-**	-	**30**	2
HD120MO_5	17	13/04/10	HD120MO	**200**	255	**210**	120	**32**	2
HD120MO_6	19	14/04/10	HD120MO	**220**	255	**200**	300	**31**	8
HD120MO_7	20	16/04/10	HD120MO	**200**	255	**200**	180	**32**	7.2
HD120MO_8	21	19/04/10	HD120MO	**200**	255	**210**	300	**87**	7
HD120MO_9	22	20/04/10	HD120MO	**200**	255	**200**	240	**36**	8
HD120MO_8def		-	HD120MO	-	-	-	-	**40**	-
HD120MO_10	23	29/04/10	HD120MO	**200**	255	**204**	360	**25**	8.1
HD120MO_11	24	30/04/10	HD120MO	**200**	255	**204**	360	**27**	8.1
HD120MO_12	25	10/05/10	HD120MO	**200**	255	**204**	360	**25**	8.1
HD120MO_13a		-	HD120MO	**-**	-	**-**	-	**39**	-
HD120MO_14	26	18/05/10	HD120MO	**200**	256	**210**	360	**88**	7
HD120MO_15	27	20/05/10	HD120MO	**200**	255	**210**	420	**29**	25.2
HD120MO_19	31	31/05/10	HD120MO	**210**	255	**210**	300	**30**	7
HD120MO_20	32	02/06/10	HD120MO	**200**	165	**210**	300	**39**	7
HD120MO_21	33	03/06/10	HD120MO	**200**	265	**210**	300	**50**	7
HD120MO_22	34	04/06/10	HD120MO	**200**	270	**210 (200)**	300	**59**	6
HD120MO_23	35	07/06/10	HD120MO	**200**	270	**210 (198)**	360	**87**	15.7

Table 3.1: Overview over all prepared samples

3.1.3 Sample Preparation for Synchrotron Measurements

Since the samples with a diameter of 8 mm were too thick for a transmission measurement they had to be reworked and milled off to about 6 mm. This process turned out to be a little tricky since the sample height is 7 mm in average being too short for processing it in the turning lathe. For this reason another way had to be found processing the γ-sample to a smaller diameter (figure 3.3). First usual α-iPP is shaped to the same diameter as the γ-sample whereas its height is not important. At the next step the two samples are pressed into sample holders for further treatment. The diameter of the cylindrical recess in the sample-holder is by 1/10 mm smaller than of the corresponding sample allowing for negligible deformation with simultaneous sufficient foothold. The two samples are welded together by a heating mirror depicted in figure 3.3c and a sample-rail (figure 3.3d) with a prism like channel ensuring that the samples are at the same height. After pressing them together for several seconds the interface of the two samples has already reached material strength and can instantly be used for further processing. Now the α-part of the welded sample is mounted at the turning lathe in which the γ-part can be milled off to the desired diameter and finally cut by the "Struers Accutom-5" saw.

(a) γ-sample and usual iPP **(b)** Sample holders **(c)** Heating mirror

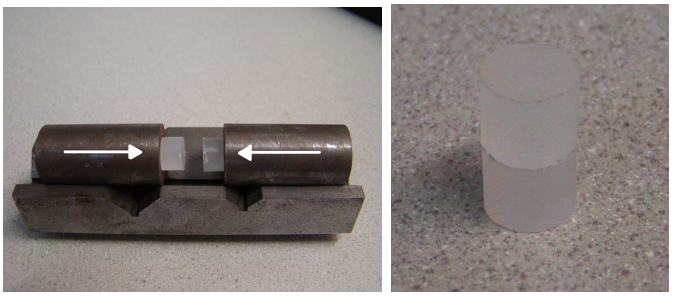

(d) Sample rail **(e)** Welded samples

Figure 3.3: Sample preparation for Synchrotron measurements

3.1.4 Preparation for DSC Measurements

The preparation for the Differential Scanning Calorimetry (DSC) -measurement is rather simple since the samples can easily be pressed out by a stamping die of a thin undeformed or deformed sample. The dimensions of the DSC-samples are about 1mm in height with a diameter of 5 mm. The measurements were performed using a "NETZSCH DSC204".

3.2 Sample Characterization

3.2.1 Differential Scanning Calorimetry - DSC

By the use of Differential Scanning Calorimetry, various parameters which are essential for the characterization of different materials can be determined, such as melting- and glass-transition-temperatures, crystallinity, phase transitions and more. In principle the emitted and/or absorbed heat quantity of a sample is measured during heating or cooling. Therefor a crucible containing the specimen and a reference cup without a sample are underlaid the same temperature program. Due to exothermic (heat flow out of the sample) and endothermic (heat flow into the sample) processes such as melting or phase transitions a difference in temperature of the sample and the reference can be observed which is related to the heat flow into or out of the sample.
For measuring the heat flow the crucibles are placed on disks with a high heat conductivity connected to thermocouples. If the temperature of the sample and the reference are the same, no difference in heat flow is observed therefore being zero. At a phase transition, the structure of the specimen changes resulting in a difference in heat flow compared to the reference sample which is proportional to the temperature difference.

Figure 3.4 shows the DSC curves for three samples with different amounts of γ-volume fraction. While the melting peak of the first measurement seems to be formed by two overlapping peaks, the graph of the second measurement does not show any evidence of this occurrence. The appearance of the double peak may be caused by the presence of two different phases α and γ respectively, due to the fact that both crystal structures have a different melting temperature. After the samples have been melt in the first heating, the γ-structure seems to be destroyed resulting in a single melting peak in the second run. In general the melting point of the samples is about 170 °C in both cases at a heating rate of 10 K/min.

3.2.2 Wide Angle X-ray Scattering using a 2D-Detector

In order to check the amount of the γ volume fraction, WAXS measurements have been carried out by the use of a 2D-Detector. As already discussed in subsection 3.1.2 it turned out to be difficult to estimate a reliable value for the amount of γ-phase by measuring in reflection. The WAXS experiments were performed on a "Bruker D8-GADDS" diffraction system by the use of CuK_α radiation with a wavelength of 0.154 nm and a spot size of the beam with 0.8 mm in diameter. Figure 3.5 shows a diffraction pattern of an iPP sample containing a high amount of γ-fraction with the corresponding line profile. Due to the homogeneous intensity distribution

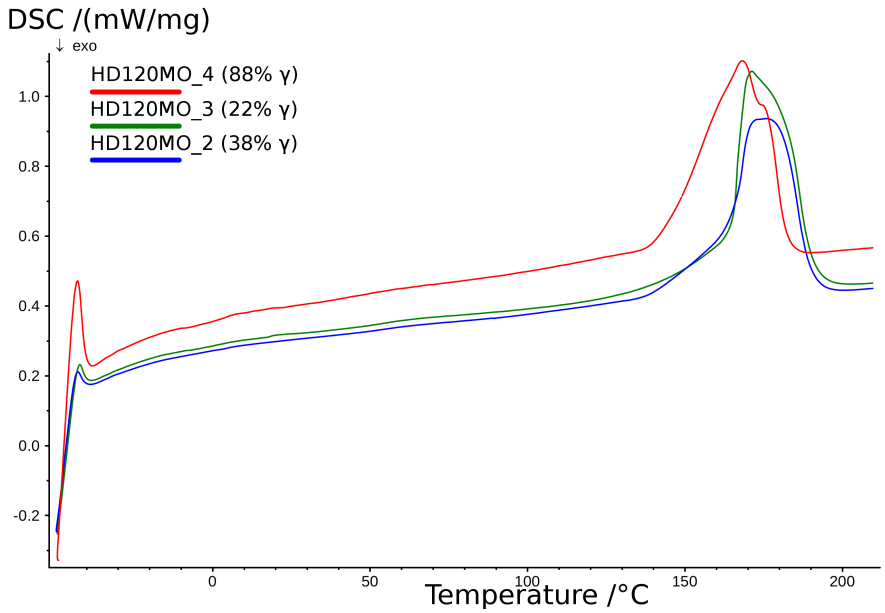

(a) First heating

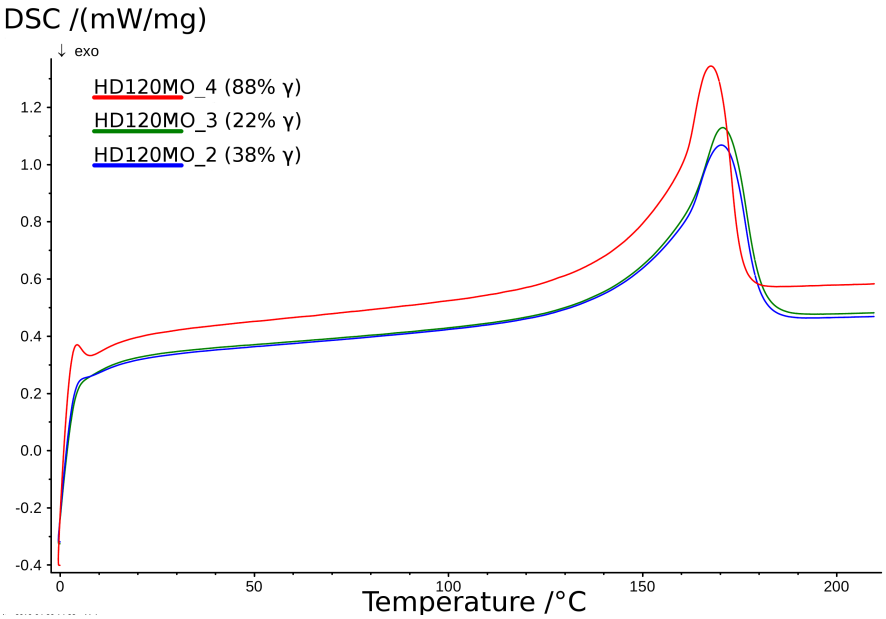

(b) Second heating

Figure 3.4: DSC measurements of samples containing a differing amounts of γ-fraction. While the first heating shows overlapping melting peaks caused by the different melting temperatures of the α- and γ-fraction, the second heating indicates only a single melting peak. Therefor, the γ-phase is melted in the first place so that only the α-phase remains in the second heating.

of the Debye-Sherrer rings it can be concluded that the material shows only weak texture. The use of an area detector is advantageous since many data points can be measured simultaneously. This provides a better statistic for the evaluation in a way that the measurement time can be reduced to 1 min which is sufficient to prove the amount of γ-volume fraction. To obtain the

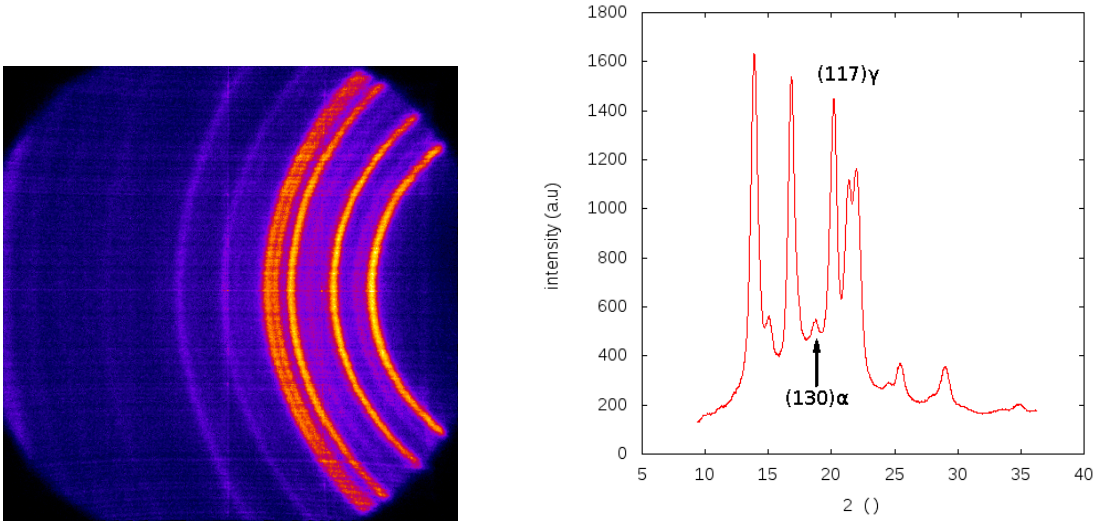

(a) Diffraction pattern of a sample with high γ-volume fraction

(b) The integral intensity from Fig. 3.5a

Figure 3.5: WAXS measurements on the "Bruker D8-GADDS"

line profile (figure 3.5b) from the 2D pattern (figure 3.5a) the intensities/counts recorded by the detector are integrated over the angles 2Θ and χ.

3.3 In-situ Deformation in Synchrotron Experiments

The WAXS measurements for the MXPA evaluation were performed at the Synchrotron Light Source ELETTRA in Trieste, Italy, on the SAXS-Beamline 5.2L. The diffraction profile was recorded using an "Inel CPS-590" position sensitive detector (figure 3.7) curved by an angle of 90 °. After recording a profile in the undeformed state the sample was deformed to different steps of compression up to 86 % of true strain while measuring in-situ under load. To ensure sufficient statistics which is necessary for a reliable evaluation, a peak to background ratio of at least 20:1 was aimed. The photon energy used for the measurement was 8 keV which corresponds to a wavelength of CuK_α radiation with 0.154 nm. The beam size was $500\mu m$ in the horizontal and $200\mu m$ in the vertical direction. The beamline 5.2L allows for a simultaneous measurement of the SAXS and the WAXS signal, but only the WAXS data were used for the evaluation in this work.

The deformation device used for the compression is optimized in geometry and power for in-situ X-ray deformation experiments (figure 3.6b). When the sample gets deformed, the beam spot will move from the center of the material in horizontal direction outwards, since the load is applied from one side by the crosshead while the other side is fixed. To ensure that the sample is always measured at the same spot, the deformation-machine is mounted at a X-Y-Table being relocated after each deformation step to the desired position.

(a) ELETTRA Synchrotron Light Laboratory

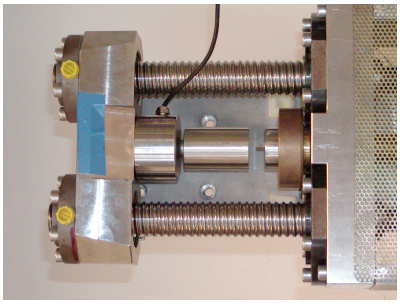

(b) Compression machine

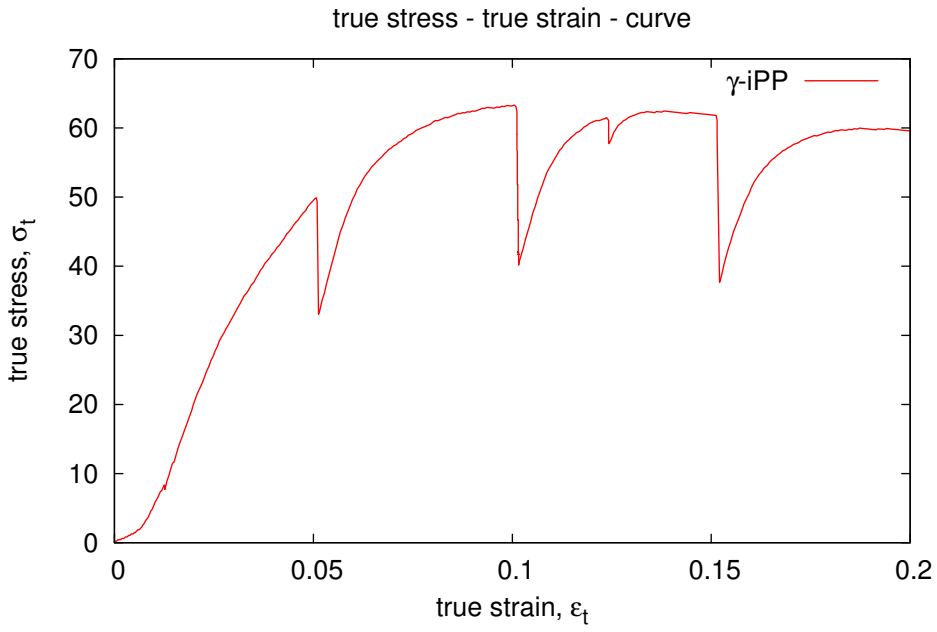

(c) Measuring positions under load. The break-ins are caused by relaxation effects

Figure 3.6

The drops in the stress-strain-curve (figure 3.6c) show the points where the measurement occurred and the crosshead was stopped. The sample was deformed to a certain strain and subsequently measured for 10 to 20 minutes, depending on the intensity of the synchrotron radiation and the thickness of the sample. During the measurement the sample had enough time to relax leading to a reduction in stress.

Figure 3.7 shows the measuring setup of the "Inel CPS-590" detector. Due to its high spatial resolution it is possible to measure at a high intensity which keeps the experimental time at a minimum.

Additionally, some profiles have been recorded by three linear detectors of the type "Braun PSD50m" located at different angles with respect to the incoming beam. It turned out that this type of detector is not suitable for polymer measurements since it tends to get overcharged by

low flux. If one compares a diffraction profile of a polymer and a metal, it appears that peaks in the polymer measurement are more broadened and have much more integral counts resulting in an increased area under the measured profile. Therefore the detector has to remove more charge at the same time if a polymer is measured. The "Braun" detector was not capable in doing so at a certain intensity. To avoid overcharging, absorber plates had to be introduced in the beam to decrease intensity.
The "Inel CPS-590" detector had no problems measuring at a high intensity and was therefore an important tool for the synchrotron experiments. Each deformation step was additionally captured by a video camera mounted next to the detector.

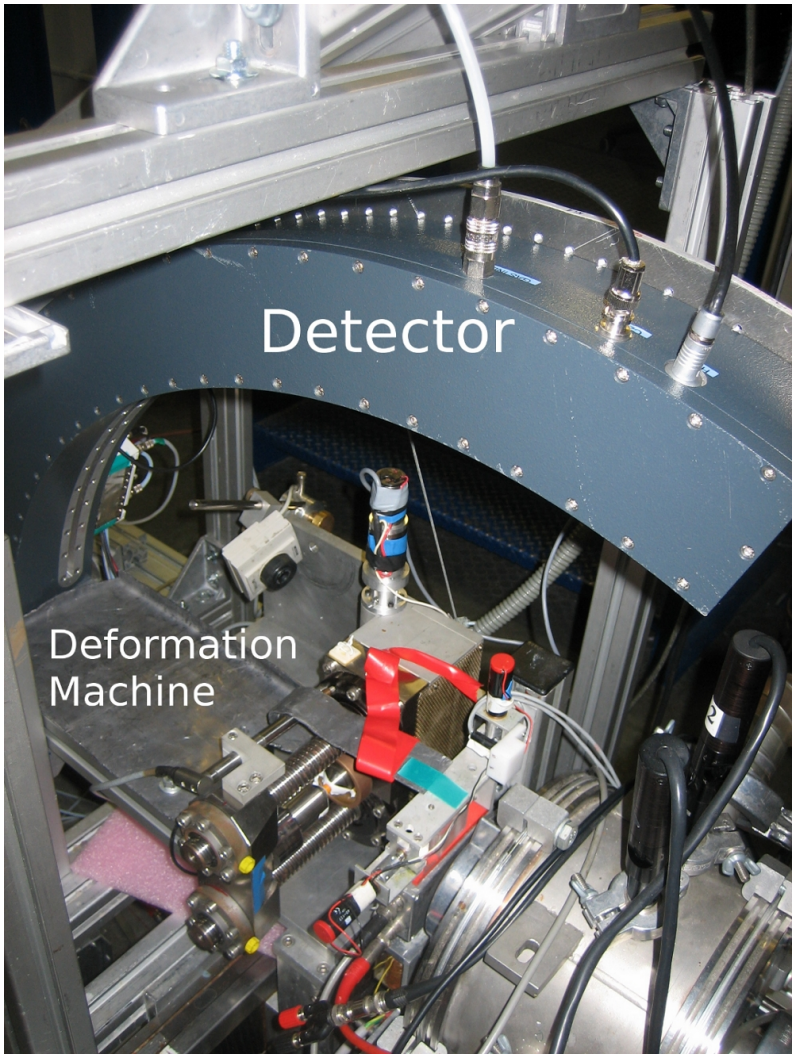

Figure 3.7: Measuring setup (Inel detector)

4. Evaluation of Experimental X-ray Line Profiles

For the evaluation of the data some assumptions have to be made which are discussed in the following chapter.

4.1 General Assumptions

(a) The samples are texture free polycrystals

(b) Every slip system contains the same amount of dislocations

(c) The Burgers-vector was fixed with 0.217 nm during the evaluation

(d) The effective outer cut-off radius R_e was kept below the CSD-size during the fitting procedure

ad (a): Semicrystalline polymers can be considered as polycrystals due to their irregular arrangement of the crystalline lamellae. During the fabrication of compression moulded plates out of α-iPP it can be assumed that a weak texture is introduced during the process. However, measurements on undeformed γ-samples by the use of a 2D-Detector revealed weak to no texture effects (section 3.2.2). The development of texture caused by the in-situ deformation experiment can not be considered during the evaluation by the MWP-program at this point.

ad (b): It is assumed that every slip system is occupied by the same amount of dislocations, independent of its orientation.

ad (c): Figure 2.5b depicts the unit cell of γ-iPP. If the possible slip system is considered to be the (001) plane and the <110> direction, a Burgers vector of 0.217 nm is a good approximation when we suppose that slip occurs along one methyl group.

ad (d): The dislocation arrangement parameter M is defined as $M = R_e\sqrt{\varrho}$ and describes the strain intensity of a given dislocation arrangement. If the M parameter is small, the correlation between the dislocations is strong resulting in sharp peaks, whereas if a high M parameter is obtained, the dislocations are distributed randomly causing rather large peak-tails (figure 4.1) [45, 42]. R_e is the effective outer cut-off radius and is determined by the strain field

of dislocations. It represents the shortest average distance when the strain field caused by a dislocation arrangement equals zero. In the case of polymer materials R_e cannot exceed the lamella thickness; thus the parameter was kept below the CSD-size during the fitting procedure.

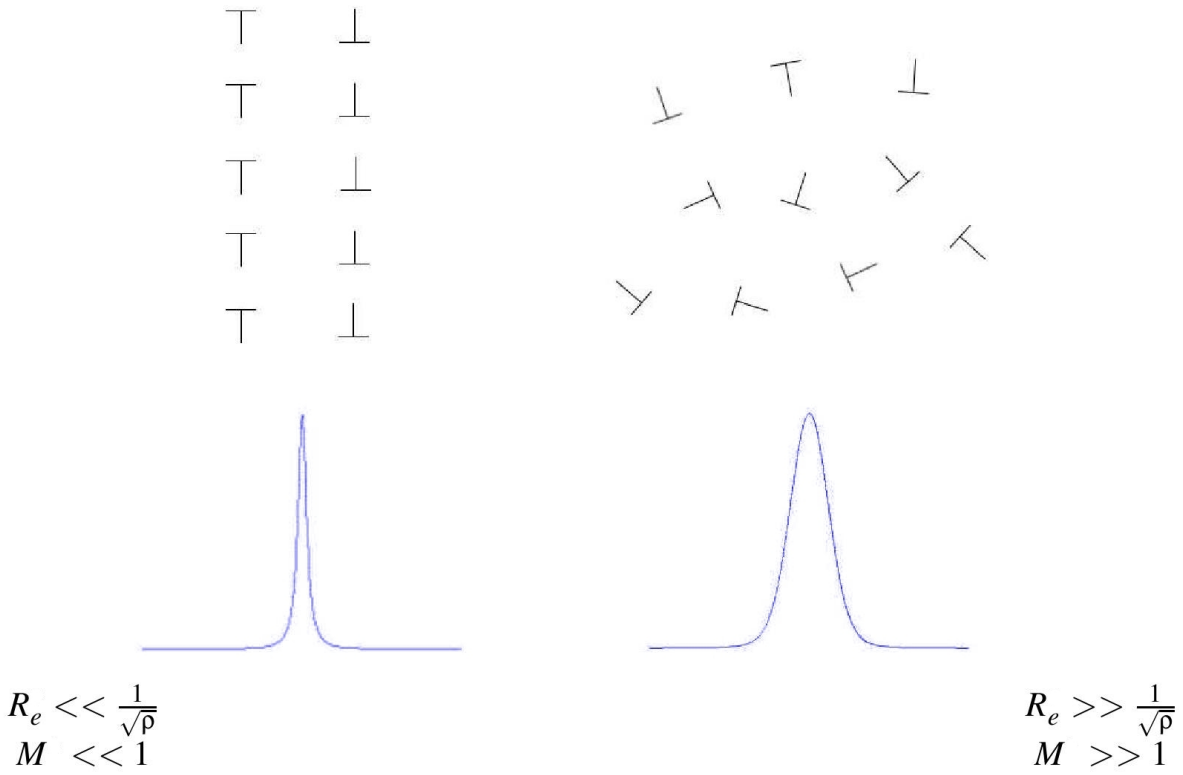

Figure 4.1: A small M indicates in a strong correlation between dislocations resulting in sharp peaks. A high M parameter points at randomly distributed dislocations resulting in large peak tails [45]

4.1.1 Peak and Phase Separation

Before the measured diffraction profiles can be evaluated, the peaks and/or phases have to be separated from each other depending on the method which is used. When applying the CMWP-Method, the diffraction patterns of the phases (i.e. the α- from the γ-phase) have to be separated since the whole phase-specific diffraction pattern is fitted in one step. On the other hand the separation of individual peaks is mandatory for applying the WH- or modified WH-Analysis, because the FWHM of each peak is plotted against k or $k\sqrt{\overline{C}}$. For a separation, the correct peak positions, the parameters for the fit-function and the background have to be known. If this is achieved a single reflection or a complete phase specific pattern can be separated by subtracting all other peaks/phases and the background from the whole diffraction profile by the use of a self-developed computer program [48].

Figure 4.2 shows a diffraction pattern of a sample containing a rather high amount of α-

modification separated into α- and γ-phases. The red line represents the measured pattern which is fitted by theoretical functions, usually a PearsonVII function for the peak and a polynomial of fifth order for the background. Additionally, supporting points for the background function can be selected in the diffraction pattern, favorably at the minimums. To achieve a better result of the background fit an additional feature for lowering and lifting of these points was implemented in the program. In general the background in polymers is relatively high compared to metals due to the high amount of amorphous phase. Particularly in samples deformed to higher strains an increase of the background can be observed.

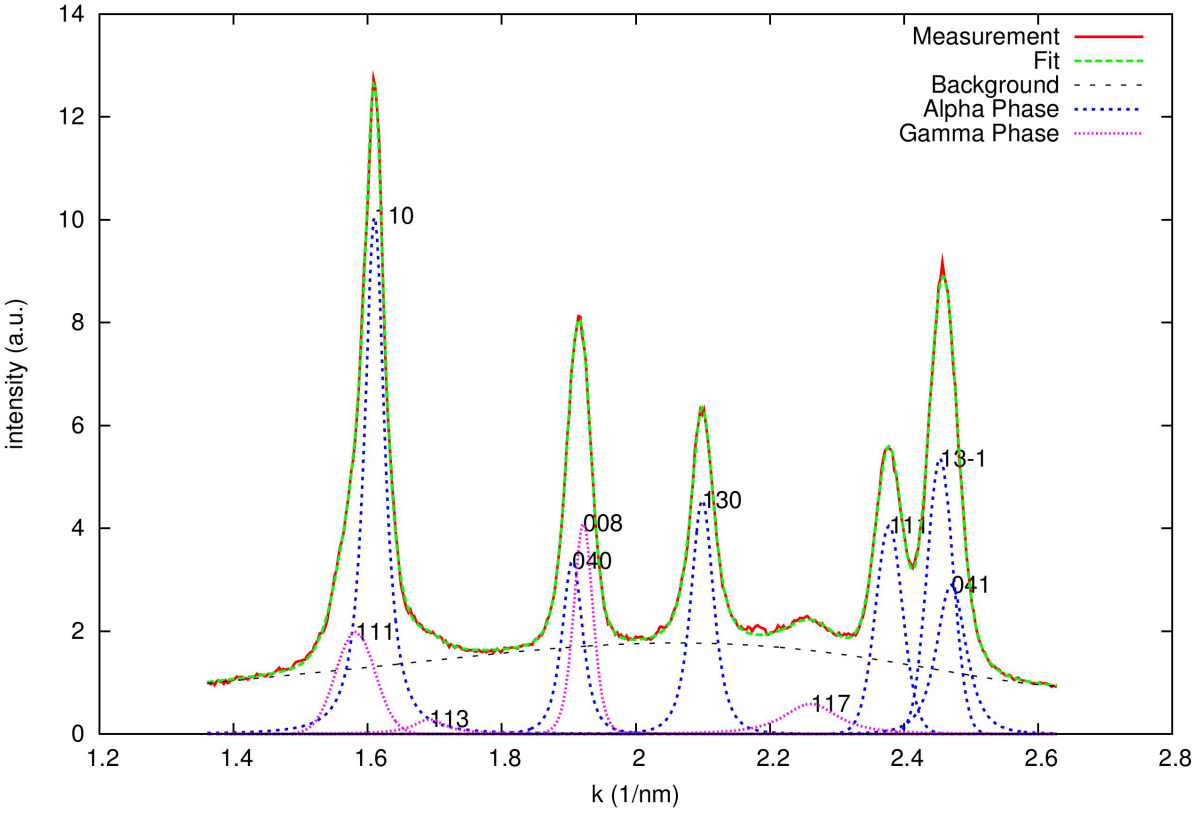

Figure 4.2: The fitted profile was separated into the α- (blue) and γ-phase (violet)

4.2 Evaluation of the WAXS-Profiles using *CMWP-fit* and the *MBK-CMWP-package*

The "MBK-CMWP-package" (M.B.Kerber - Convolutional Multiple Whole Profile - package [49]) is a program which allows for a more accurate evaluation of the measured data by means of "CMWP-fit". The principle of the package is that different starting values of each parameter such as dislocation density, cut-off radius, ellipticity are varied over all possible permutations and are used for the evaluation by "CMWP-fit". Additionally the fit parameters for the dislocation contrast factor $(a_1 \cdots a_n)$ can be either fixed or varied from profile to profile.

The evaluation of a diffraction profile can be divided into three different steps:

(i) The peak and/or phase separation

(ii) The pre-evaluation by the use of CMWP-fit

(iii) Applying the MBK-CMWP-package on CMWP-fit

Step (i) was already discussed in 4.1.1, but it should be emphasized that in this work only the diffraction patterns of the phases, more exactly of the α- and γ-phase, have been separated from each other and not the individual peaks because "CMWP-fit" uses the whole pattern for the fitting procedure.

Step (ii) is very important for a first estimation of the fit-parameters such as dislocation density, dislocation contrast factors, the outer cut-off radius etc. which can be used as reference points for the "MBK-CMWP" evaluation. Additionally the background is reduced since it turned out that the background subtraction in the phase separation process is too small. If the parameters are estimated for each recorded profile the results should be saved together in one file which is necessary for applying the MBK-CMWP-package.

In step (iii) the starting parameters for b (median of the grain-size distribution), c (standard deviation), d (dislocation density), e (outer cut-off radius) and epsilon (ellipticity) are set in the file

```
multieval_ortho.
```

It is reasonable to use, beside the value obtained by the pre-evaluation procedure, a lower and an upper value e.g. if the pre-evaluation leads to $d = 50$ for the dislocation density one should use additionally 25 and 75. More than 4 starting values for each parameter should not be set, otherwise the evaluation process becomes time consuming since every value from the different parameters is combined with each other. Of course the calculation time also highly depends on the computational power and the number of free parameters. During the calculation of the results presented in chapter 5 the parameters b,c and d were varied by two to three different values while the parameter e and epsilon where set at the value obtained by the pre-evaluation. The fit-parameters for the dislocation contrast factor ($a_1 \cdots a_5$) were once adapted to each profile and fixed at a certain value in the second and third run. In the case of individual contrast-fit-parameters, a file called

```
*.fit.ini.fix
```

with the corresponding a_i has to be started for every profile. If all desired values and parameters are set the evaluation is started by the command

```
./multieval_ortho $filename of the profile$.
```

When the computation is finished the averages of the results including error bars are calculated from each profile by the command:

```
make_sreies_results.sh $filename.ini$.
```

A small error bar indicates well converging results arising from the different starting values, which can be interpreted as a reliable output. In the case of large error bars the results differ from each other more significantly e.g. as a result of inappropriate values of the contrast-fit-parameters (for details see chapter 5).

5. Results and Discussion

The following results are discussed by the example of material HD120MO_23 containing 87 % of γ-modification (see table 3.1). The profiles were measured in-situ under load using synchrotron radiation and have been evaluated by the MXPA- and modified Williamson-Hall Method.

5.1 Evolution of the Microstructure

5.1.1 Diffraction Profiles

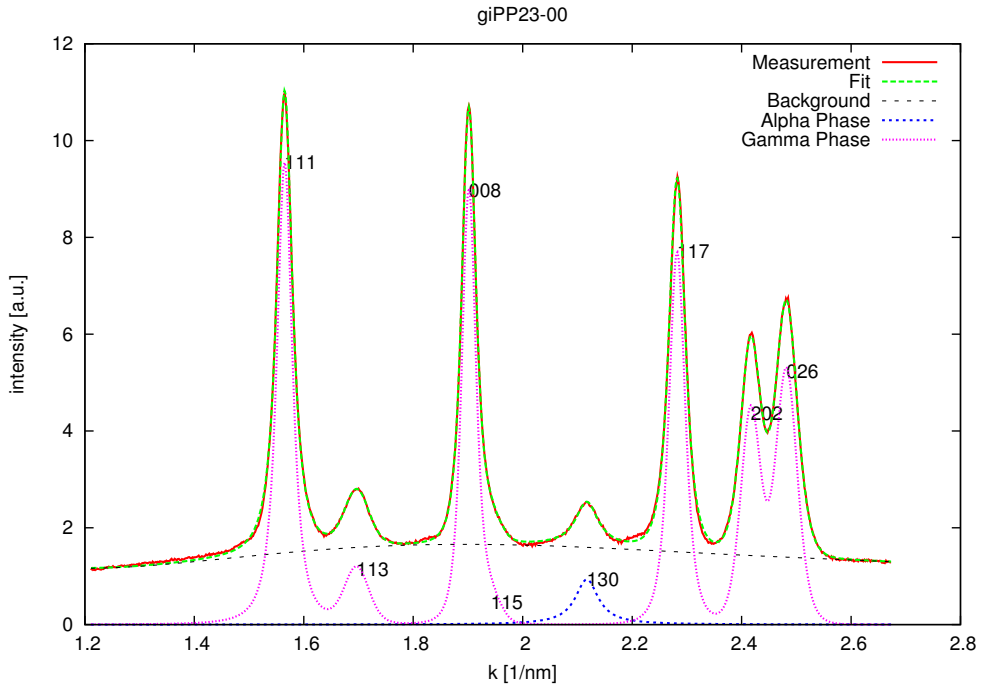

Figure 5.1: Diffraction profile of the undeformed sample

Figure 5.1 shows the diffraction profile of the undeformed sample, figure 5.2 of the sample deformed to $\varepsilon_{true} = 86$ % measured in the in-situ compression experiment. One of the main differences of the two profiles is the higher peak broadening at the deformed sample which can be related to a formation of dislocations on the one hand and/or to a decrease of the CSD-size on the other hand. It will be shown that the generation of dislocations plays a minor role in γ-iPP compared to the broadening caused by size effects. It can also be observed that the intensity of the background remains nearly at a constant level while the intensity of the peaks decreases.

Especially the (026) reflection changes from an intensity of initially 5.0 [a.u.] to about 1.0 [a.u.] while its neighbouring (202) peak slightly increases from about 4.5 to 5.0 [a.u.]. These changes in peak intensity could be related to texture effects, but also to the increasing absorption since the sample becomes thicker at higher loads.

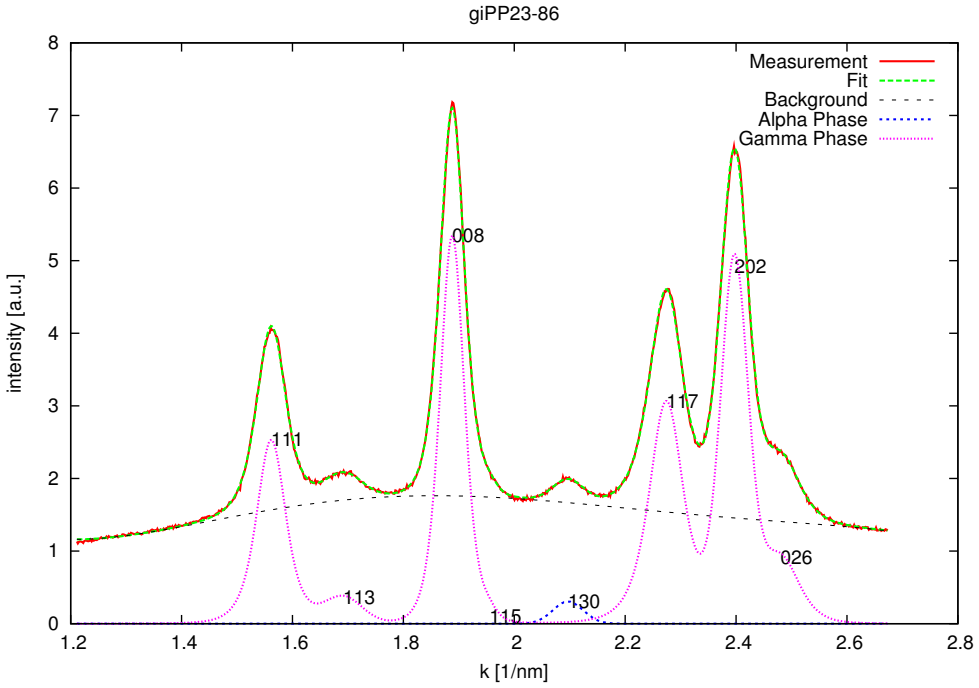

Figure 5.2: Diffraction profile of the sample deformed to 86 % of true strain indicating an increased peak broadening

5.1.2 Crystallinity

A continuous decrease in crystallinity from initially 50% to 39% can be observed with increasing strain (figure 5.3). This behavior is caused by the formation of shear bands. Lezak et al. [13] provided evidence for a development of shear bands already at the yield within the amorphous phase. Those shear bands duplicate rapidly with increasing load and spread over the whole sample volume resulting in heavy defragmentation of the lamellae which leads to a decrease in crystallinity.

5.1.3 Fit Parameters of the Dislocation Contrast Factor

In order to evaluate parameters such as dislocation density, CSD-size etc. a pre-evaluation has been executed for determining the fit-parameters of the dislocation contrast factors. This is achieved by taking reasonable starting values from the modified Williamson-Hall analysis which are refined in the following fitting procedure. Figure 5.4 shows the fit parameters $a_1 \cdots a_5$ obtained from the pre-evaluation using CMWP-fit. One can see that the absolute value decreases at higher strains i.e. the parameter a_4 changes from initially 430 at $\varepsilon = 0\%$ to 210 at $\varepsilon = 86\%$. This occurrence is a strong indication for a change in the dominant dislocation character [38].

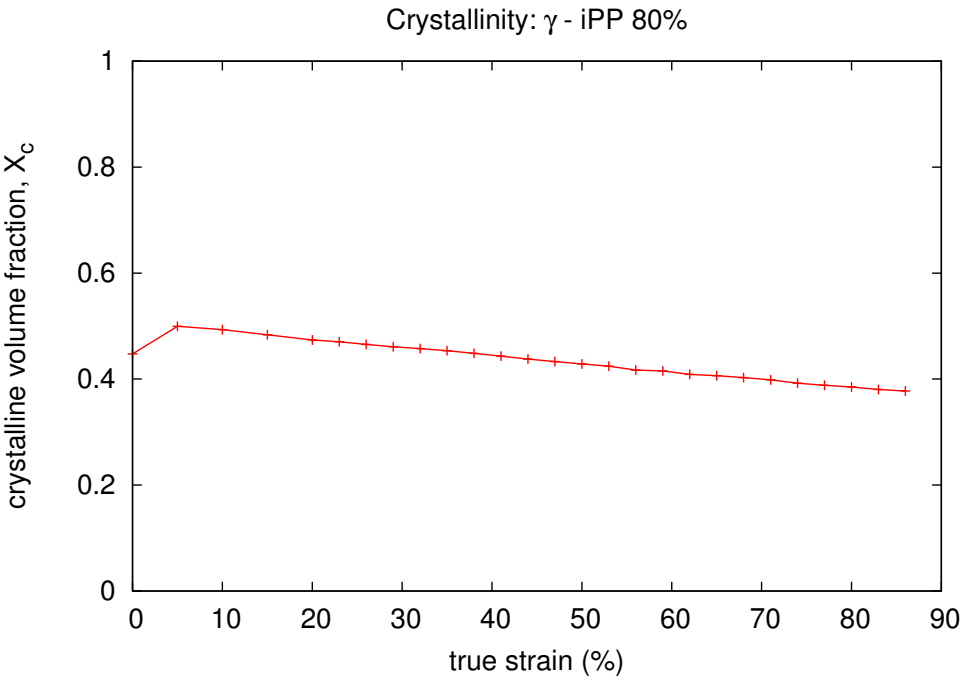

Figure 5.3: The decrease in crystallinity is caused by the formation of shear bands which start to multiply at higher strains and lead to a defragmentation of the crystalline lamellae

After obtaining the starting values the MBK-CMWP package was used for further evaluation.

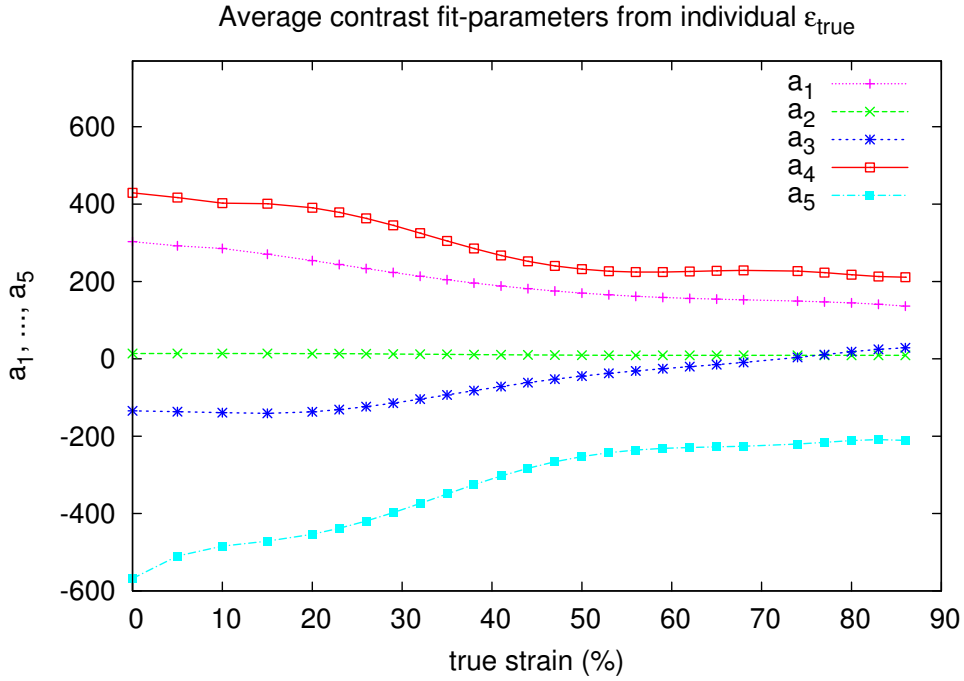

Figure 5.4: The individual fit-parameters of the dislocation contrast factor for each deformation step obtained by the use of CMWP-fit

To check if there is a significant effect on the final result by applying either fixed or variable

contrast fit-parameters, three different arrangements of the fit-parameters a_i were used for the evaluation:

(i) The "a_i" values from the sample deformed to 32% were applied to all profiles for the evaluation

(ii) The "a_i" values from the sample deformed to 77% were fixed for all profiles

(iii) The individual contrast fit-parameters from each deformation step were applied to the corresponding profiles

These three evaluation steps are depicted in Figure 5.5 by means of the fit-parameter a_4. The upper straight line represents the value for a_4 taken from the 32% sample. It can be seen that this value has been applied to all other profiles for the evaluation. The lower line represents the fixed value obtained from the sample deformed to 77%. The third evaluation was carried out by using the characteristic fit-parameters for each profile, which can also be seen in Figure 5.4 where all a_i are depicted.

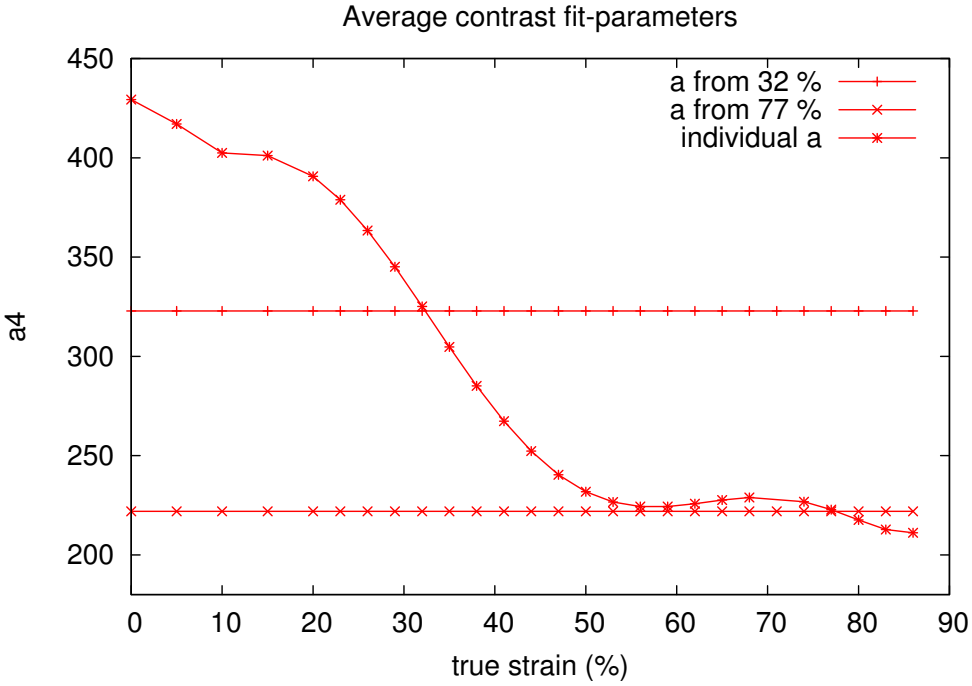

Figure 5.5: Contrast fit parameters for the three different evaluations using the parameter a_4. The two straight lines represent the fixed fit-parameters obtained from the sample deformed to 32% and 77%. The curved line shows that the individual fit parameter from the corresponding deformation step was used as depicted in figure 5.4

5.1.4 Ellipticity

One of the parameters obtained by the MBK-CMWP evaluation is the ellipticity ϵ, indicating the geometric shape of a crystal as already discussed in chapter 2 / 2.5.4.

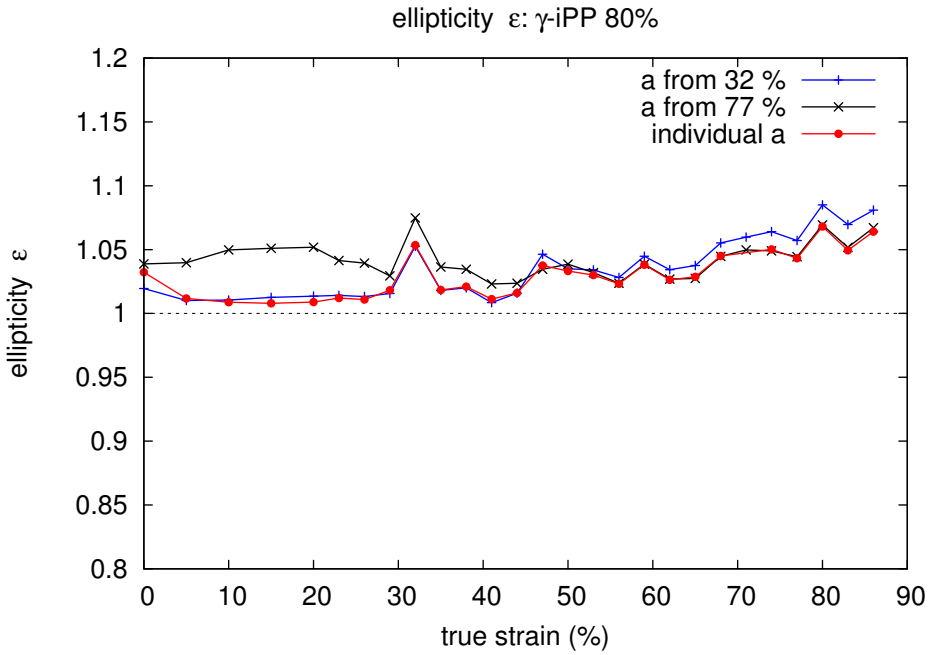

Figure 5.6: The cross section of the crystalline lamellae becomes more elliptical at higher strains

The red "individual" curve in Figure 5.6 illustrates a change in ellipticity from about 1 to 1.07 at higher strains which is a change of 7%. An explanation of the development of the ellipticity with increasing strain will be given in section 5.2.

5.1.5 Dislocation Density and Residuals

The consequences of the fit parameters for the dislocation density, and the residuals, representing the difference between the measured and the fitted data are shown in Figure 5.7 and 5.8 respectively. The residuals from the 77% sample are very high at lower strains, which seems reasonable since the fit parameters change significantly during the compression experiment according to Figure 5.4. The high residuals at low deformations reflect in large error bars in the dislocation density. At a true strain of 53% the residual decreases resulting in lower error bars in the dislocation density.

It is to mention that the magnitude of the error bar does not represent the physical error of the measurement, instead it is a measure of the reproducibility or robustness of the fit. For example a low error bar means that different starting values (in this case for the dislocation density) converge well to a certain value.

The same is true for the 32% sample where low residuals can be observed at lower strains leading to smaller error bars at the beginning of the deformation which increase at higher

strains caused by a change in the residuals.

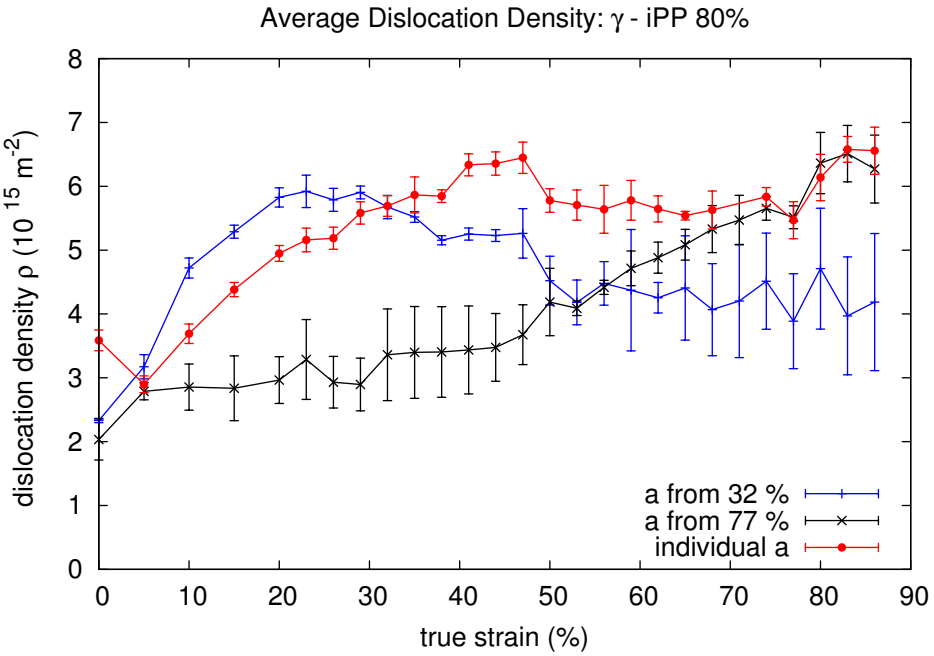

Figure 5.7: Dislocation density development of the γ-modified sample. After a slight increase of the dislocation density at the beginning of deformation it stays almost constant reaching a true strain of 35%.

In contrast to that, the curve of the individual fit parameters shows low residuals over all steps of deformation meaning that a good fit was achieved using those parameters, which reflects in low error bars in the dislocation density over all profiles. Figure 5.7 demonstrates how important a correct determination of the dislocation contrast factor is, especially if it changes significantly over various steps of deformation the individual fit-parameters should be taken into account in order to minimize the sources of error.

The red curve concerning the development of the dislocation density is the final result of the evaluation. A slight increase from 3×10^{15} to 6.5×10^{15} can be observed at the beginning of deformation, but stays at a constant level reaching a true strain of 35% and can therefore be considered as almost constant over all steps of deformation.

The final result of the dislocation density development is compared to the dislocation density curve from α-iPP [2] (Figure 5.9). The reason why the evaluation was just carried out up to a true strain of 45% in α-iPP is that no satisfying fit could be achieved at the profiles measured at higher strains since a different detector was in use compared to the measurements of the γ-sample. However, the data could be well evaluated from lower strains which is sufficient to draw a comparison between the two phases in isotactic Polypropylene.

As already mentioned before, the dislocation density in γ-iPP weakly increases preferably at the beginning of deformation, but then stays constant from 35% of deformation upwards. In contrast to that, the dislocation density in α-iPP increases much more significantly. A change

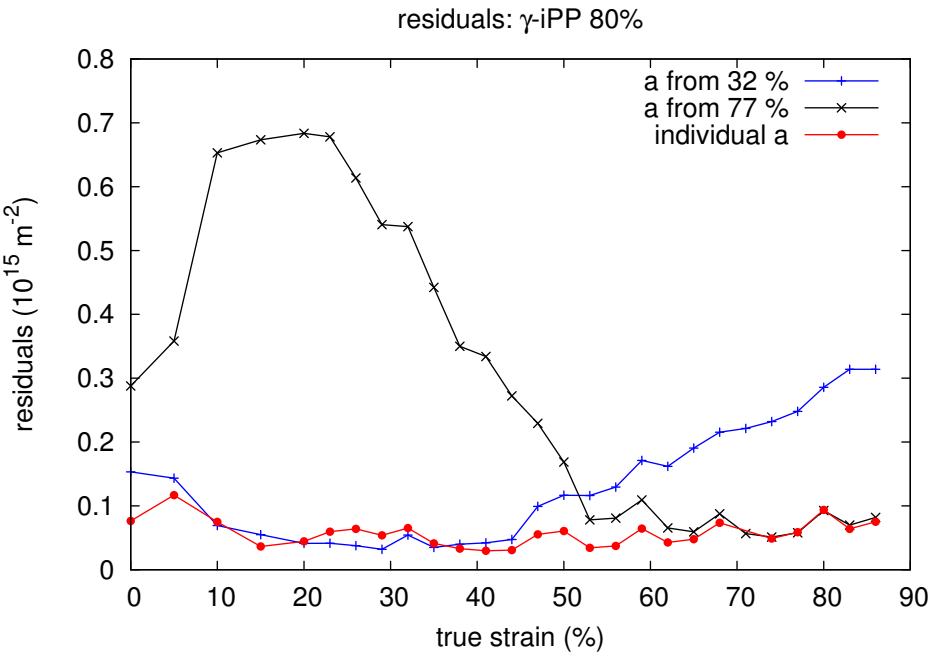

Figure 5.8: The residuals obtained from the three different evaluations.

from initially 0.5×10^{15} to 1.2×10^{16} is observed within the first 45% of deformation, which seems to be a different mechanism of plastic deformation to occur in α-iPP compared to γ-iPP.

One has to distinguish between grown-in and mobile dislocations. In the case of α-iPP the main deformation mechanism is the intralamellar slip within a crystal which is accompanied by a dislocation generating process (see section 2.4). These dislocations are mobile dislocations since they can move through the crystalline phase under deformation. A possible explanation for the dislocation density development in γ-iPP could be that "misfit" dislocations which are a kind of grown-in dislocations play a major role. This model will be explained in detail in section 5.2. However, since the molecular structure of the γ-phase consists of non-parallel chains (as already discussed in chapter 2.1 and 2.4), the possible slip systems are confined. The critical resolved shear stress (CRSS) which is necessary to activate a slip system seems to be too high so that no mobile dislocations are generated resulting in an interlamellar shear of the amorphous layers.

5.1.6 Lamellae Thickness

Another parameter of interest is the coherently scattering domain size (CSD-size). It represents the smallest coherently scattering size in a crystal which can be related to the lamellae thickness in polymers (refer to 2.5.4). Figure 5.10 compares the lamella size of the α and γ-modification with respect to the true strain. It can be seen that the lamellae of the γ-phase are in average about 10nm larger than those of the α-phase. An interesting fact is that a marked reduction of the lamellae size can be observed in both, the γ- as well in the α-sample. A possible explanation

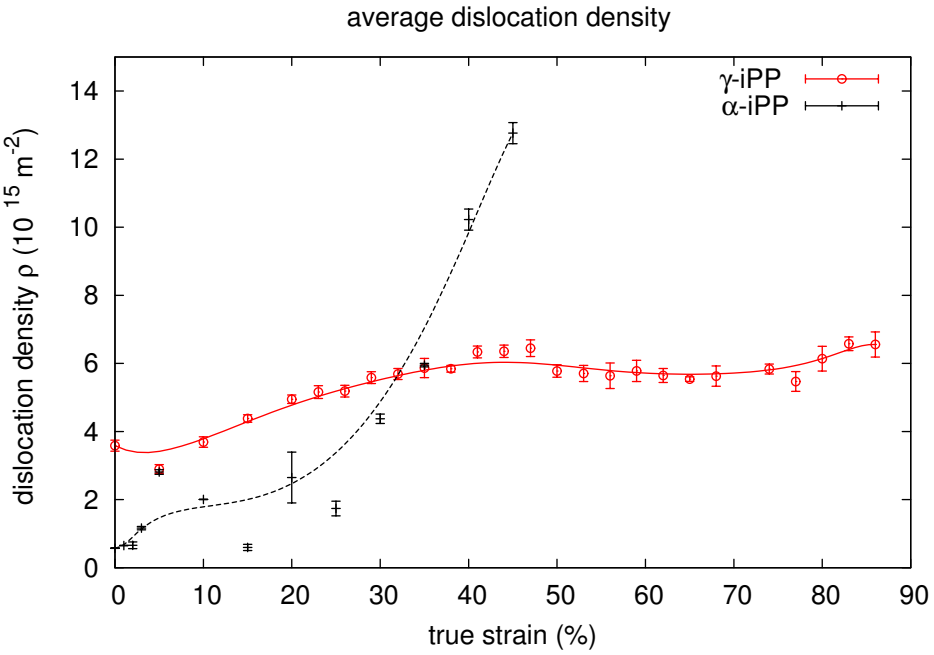

Figure 5.9: Comparison of the dislocation density development of α- and γ-iPP. While the dislocation density increases by a factor a 10 within the first 45% of deformation in the α-sample it stays almost constant in the γ-modified sample pointing at a different deformation mechanism

of this reduction is given in section 5.2. The error bars of the CSD-size are in the order of the symbol size which indicates well converging starting parameters and therefore reliable results. Except the lamella size of the undeformed sample, which seems to be improbable since it is located between 35 and 40nm.

5.1.7 Stress - Strain - Curve

The stress-strain-curve in Figure 5.11 presents the in-situ deformation curve during the WAXS-measurement at the synchrotron for the γ- (red full line) and α-sample (black dashed line) respectively. The enhanced strength of the γ-phase can be related to the fact that only one slip system is allowed which needs a higher CRSS to be activated or to the marked difference in lamellae size. The softening of the γ-sample may be caused by the relatively low crystallinity in contrast to other polymers, which lead to a decrease in strength. Another reason could be the long crystallization time. The samples have been crystallized for 4 - 6 hours resulting in a re-entanglement of the macromolecular chains in the amorphous phase and further in a lower strength as well.

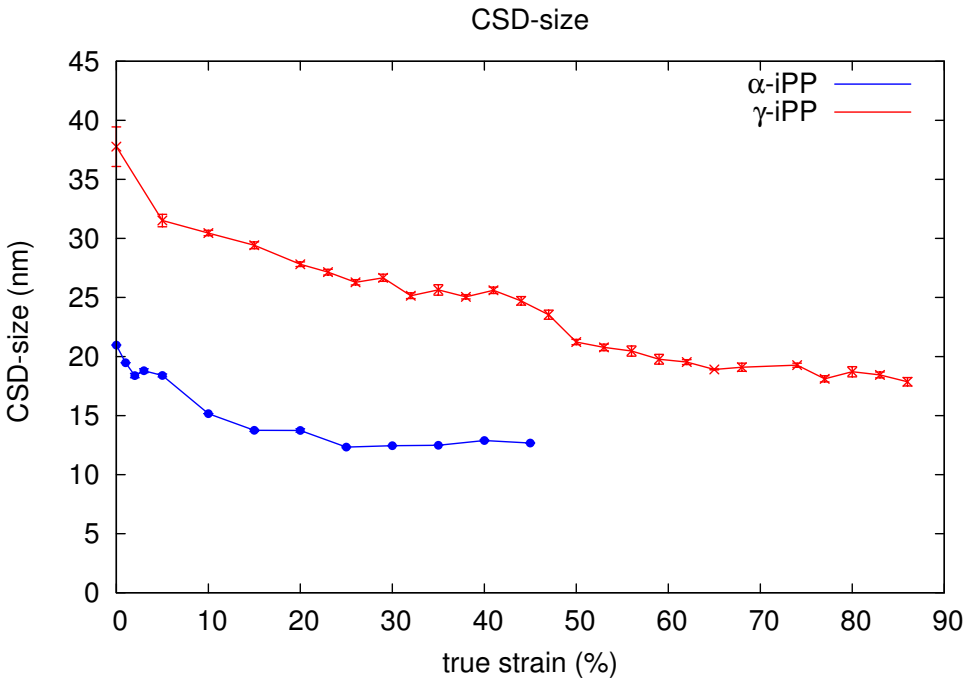

Figure 5.10: Lamellae thickness of α- and γ-iPP. The decrease in lamellae thickness is caused by the formation of shear bands cutting through the crystalline phase.

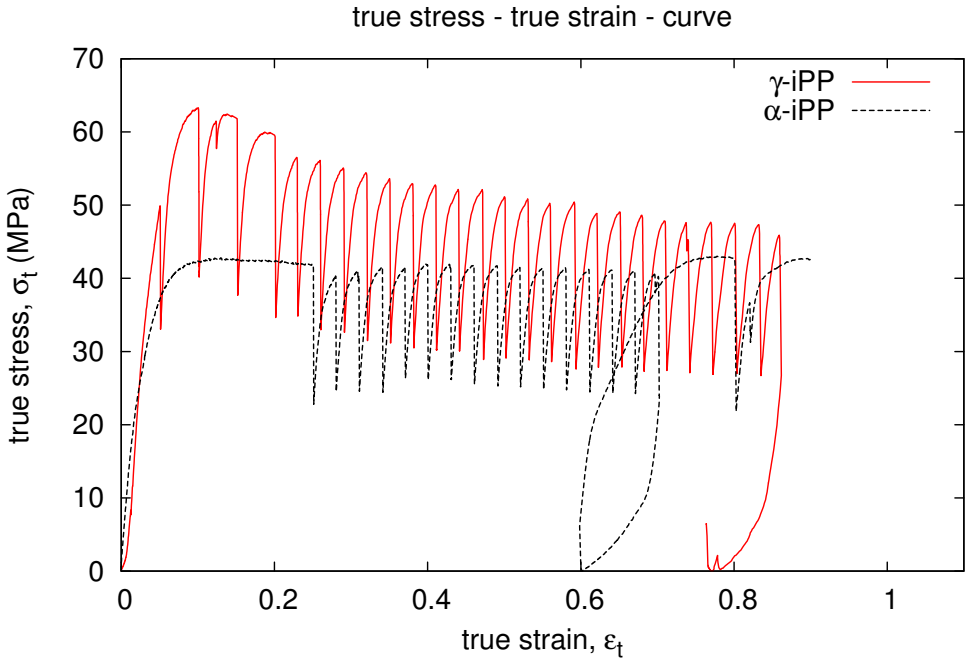

Figure 5.11: True-stress true strain curve of γ-iPP (full line) and of α-iPP (dashed line). The enhanced strength points at different deformation mechanisms in the two phases.

5.2 Possible model explanation: misfit dislocations

The behaviour of the dislocation density and CSD-size as a function of the applied strain can be explained in terms of misfit dislocations.

Rather then a single crystal straightened in a certain direction, the lamellae can be imagined as an aggregate of crystalline blocks with small differences in the relative orientation. If the misorientation between two blocks exceeds an angle of about 1.5°, the two parts are interpreted as individual coherently scattering domains by the MWPA-method (figure 5.12).

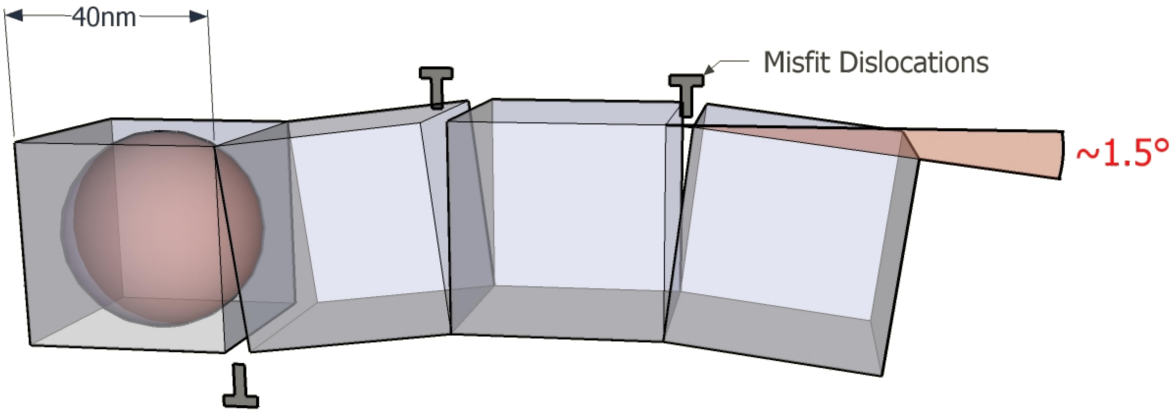

Figure 5.12: Schematic drawing of a lamella consisting out of crystalline blocks. Misfit dislocations are present in the interface of the blocks.

It is expected that grown-in dislocations such as misfit dislocations [50] are present between the boundaries of the crystalline blocks. When deformation occurs, the lamellae start to bend leading to a further fragmentation of the crystalline blocks and thus a decrease of the CSD-size (figure 5.13). If we imagine a decrease of the CSD-size by 50% meaning that twice as many blocks are produced by fragmentation, the total area between those blocks has to increase by a factor of 2. Since misfit dislocations are located in the block boundaries, the dislocation density has to increase by a factor of 2 as well. This behavior could be observed in our measurements (figure 5.10 and figure 5.9) and is described by [50]

$$\Theta = 2 \cdot \arcsin \frac{b \cdot L \cdot \varrho}{2} \tag{5.1}$$

5.1 describes the relation between the angle Θ of two adjacent blocks and the density of dislocations ϱ located in the interfaces of the adjacent blocks. Other parameters are the Burgers vector b and the block size L.

By the use of this equation, the development of the CSD-size and dislocation density from section 5.1 can be explained. Especially, if an angle of $\Theta = 1.5°$ is assumed the experimental value of the CSD-size is obtained by inserting the experimental value of the dislocation density and vice versa.

Figure 5.10 depicts a decrease of the CSD-size from approximately 40nm to 20nm. If we consider Θ to be constant, the dislocation density is forced to get twice as large which could be observed according to figure 5.9 (the dislocation density increases from 3×10^{15} to 6.5×10^{15} $[1/m^2]$).

If we transform equation 5.1 for L, the block size can be calculated by a rough approximation using the Burgers vector $b = 0.217nm$ and the angle between two blocks $\Theta = 1.5°$:

At the beginning of deformation the dislocation density equals 3×10^{15} $[1/m^2]$ resulting in a block size of

$$L(\varepsilon_t \approx 0) = \frac{2 \cdot \sin\frac{\Theta}{2}}{b \cdot \varrho} = \frac{2 \cdot \sin(0.75)}{(0.217 \cdot 10^{-9}) \cdot (3 \cdot 10^{15})} = 40nm$$

With increasing deformation the dislocation density rises up to 6×10^{15} $[1/m^2]$ leading to

$$L(\varepsilon_t > 0.35) = \frac{2 \cdot \sin\frac{\Theta}{2}}{b \cdot \varrho} = \frac{2 \cdot \sin(0.75)}{(0.217 \cdot 10^{-9}) \cdot (6 \cdot 10^{15})} = 20nm$$

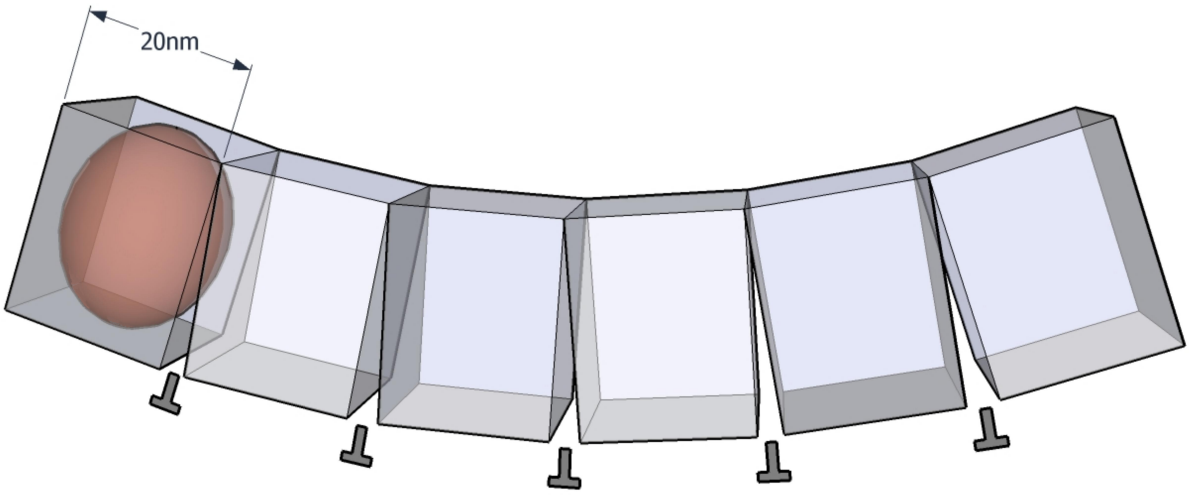

Figure 5.13: The lamella starts to bend when deformation occurs leading to a fragmentation of the crystalline blocks and a decrease in the CSD-size

This model explains that misfit dislocations are a type of grown-in dislocations which are not mobilized under deformation and therefore not essential for the plastic deformation of the γ-phase in iPP. However, misfit dislocations can be considered as a geometrical necessity, generated by the bending of the lamellae under deformation.

6. Summary and Conclusions

IPP samples with a high amount of γ-phase have been produced by the use of a special experimental setup. A pressure of at least 200 MPa was provided by a pressure cell mounted to a universal testing machine. The necessary crystallization temperature of 210 ℃ was achieved by a heating tape attached to the upper part of a specially designed pressure chamber.
In-situ X-ray deformation experiments have been carried out with a sample containing 80% of γ-phase at the synchrotron ELETTRA in Trieste, Italy. In order to obtain a detailed development of the microstructural parameters, several profiles have been recorded during small deformation steps reaching from the initial state up to a deformation of 86%. The evaluation which was carried out by means of the MXPA- and Modified Williamson-Hall-Method, reveals a presence of dislocations and a slight increase of the dislocation density in the early stages of deformation, but remains constant from a true strain of 35%. The increase of the dislocation density can be explained by the generation of misfit dislocations located in the boundaries between crystalline blocks. Since the amount of blocks and their interfaces multiply with increasing strain, the same has to be true for the dislocation density. The evaluation of the CSD-size shows relatively thick lamellae in the case of γ-iPP, possibly resulting from the long crystallization time of 4 to 6 hours. However, a decrease of the lamellae thickness was observed with increasing strain in α- as well as in γ-iPP. The decrease of the CSD-size in γ-iPP is caused by a bending of the lamellae leading to a fragmentation of the crystalline blocks. An equation is presented allowing for an approximation of the block size at a known dislocation density and is therefore a first proof for the reliability of the model. A true stress - true strain curve of the in-situ X-ray deformation experiment was recorded indicating an enhanced strength of the γ-phase. The increased yield stress is either caused by the higher CRSS in the possible slip system, from the thicker lamellae or from both.
In summary it can be said that γ-samples have been measured in-situ under X-ray deformation at the synchrotron showing a slight increase in dislocation density probably caused by geometrical necessary misfit dislocations generated in the boundaries between the crystalline blocks due to the bending of the lamellae.
This work gives rise for further investigations of the microscopic mechanisms being active during plastic deformation in γ-iPP. The presented model involves a number of assumptions which can be verified by various experimental techniques e.g. the tilt angle of the crystalline blocks could be measured by SEM. Another question is why the ellipticity does not increase by a factor of

2 when the CSD-size decreases by the same extent. Additionally, solution grown γ-iPP single crystals could be investigated in order to check if the behavior of the dislocation density with respect to the applied strain is similar to semi-crystalline γ-iPP. Particularly the generality of the presented misfit dislocation model could well be tested in such a system.

7. Appendix

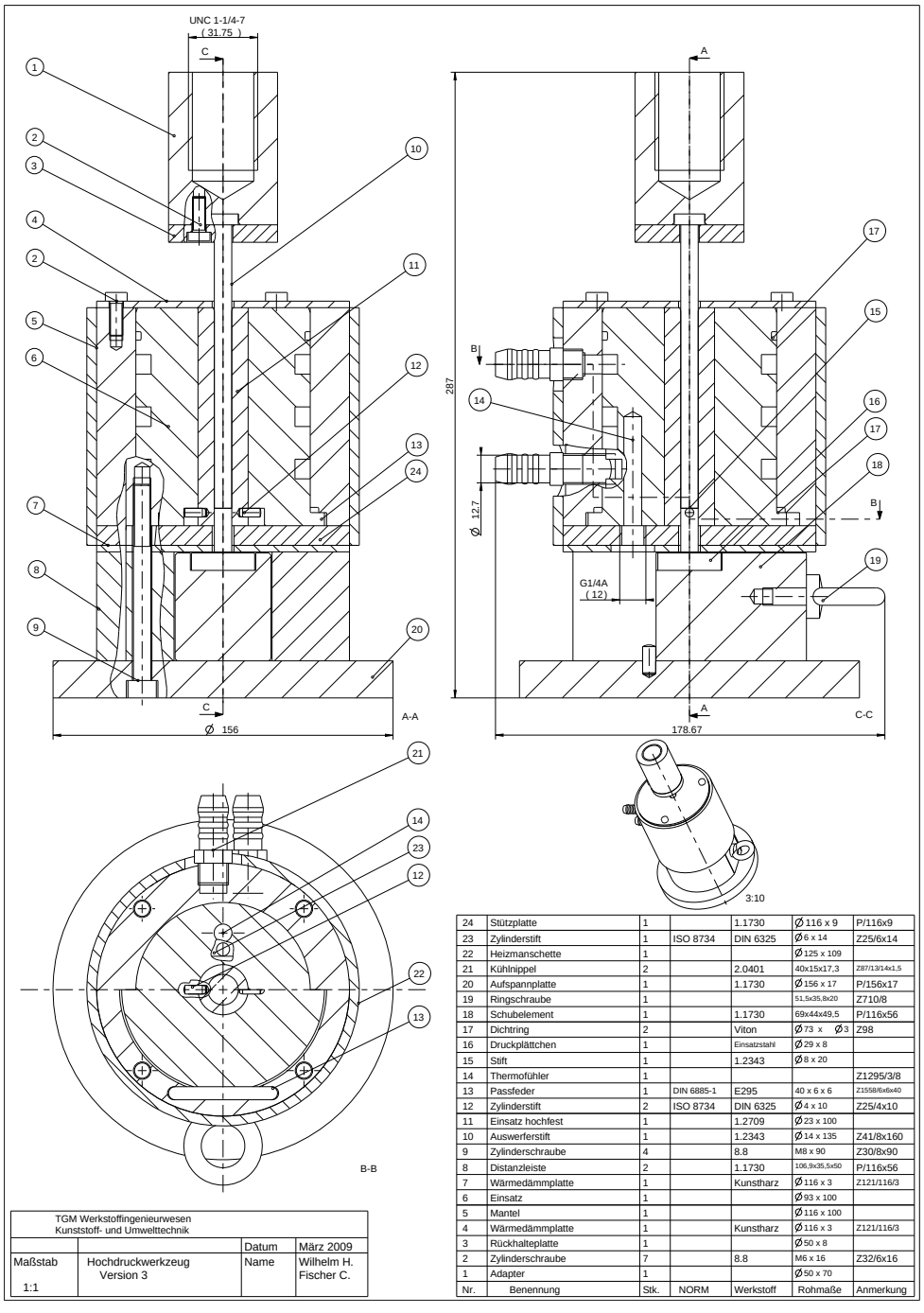

24	Stützplatte	1		1.1730	Ø116 x 9	P/116x9
23	Zylinderstift	1	ISO 8734	DIN 6325	Ø6 x 14	Z25/6x14
22	Heizmanschette	1			Ø125 x 109	
21	Kühlnippel	2		2.0401	40x15x17,3	Z87/13/14x1,5
20	Aufspannplatte	1		1.1730	Ø156 x 17	P/156x17
19	Ringschraube	1			51,5x35,8x20	Z710/8
18	Schubelement	1		1.1730	69x44x49,5	P/116x56
17	Dichtring	2		Viton	Ø73 x Ø3	Z98
16	Druckplättchen	1		Einsatzstahl	Ø29 x 8	
15	Stift	1		1.2343	Ø8 x 20	
14	Thermofühler	1				Z1295/3/8
13	Passfeder	1	DIN 6885-1	E295	40 x 6 x 6	Z1558/6x6x40
12	Zylinderstift	2	ISO 8734	DIN 6325	Ø4 x 10	Z25/4x10
11	Einsatz hochfest	1		1.2709	Ø23 x 100	
10	Auswerferstift	1		1.2343	Ø14 x 135	Z41/8x160
9	Zylinderschraube	4		8.8	M8 x 90	Z30/8x90
8	Distanzleiste	2		1.1730	106,9x35,5x50	P/116x56
7	Wärmedämmplatte	1		Kunstharz	Ø116 x 3	Z121/116/3
6	Einsatz	1			Ø93 x 100	
5	Mantel	1			Ø116 x 100	
4	Wärmedämmplatte	1		Kunstharz	Ø116 x 3	Z121/116/3
3	Rückhalteplatte	1			Ø50 x 8	
2	Zylinderschraube	7		8.8	M6 x 16	Z32/6x16
1	Adapter	1			Ø50 x 70	
Nr.	Benennung	Stk.	NORM	Werkstoff	Rohmaße	Anmerkung

TGM Werkstoffingenieurwesen Kunststoff- und Umwelttechnik			
		Datum	März 2009
Maßstab 1:1	Hochdruckwerkzeug Version 3	Name	Wilhelm H. Fischer C.

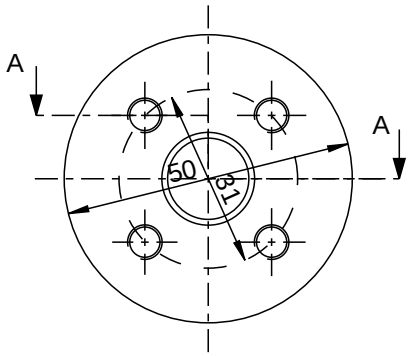

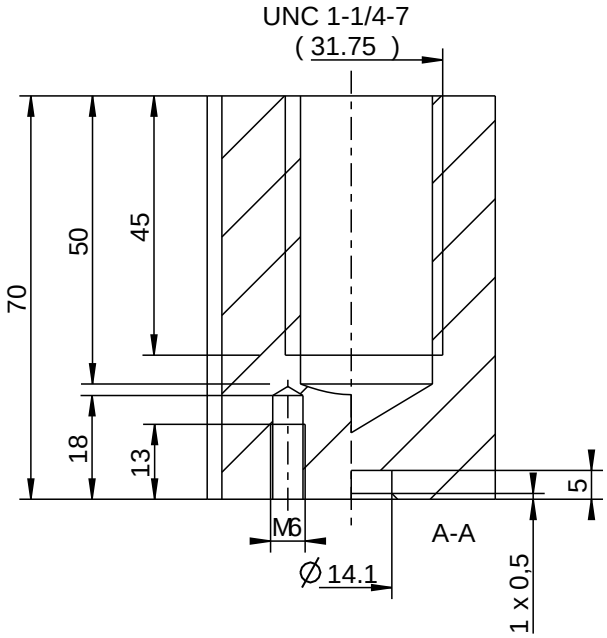

TGM Werkstoffingenieurwesen Kunststoff- und Umwelttechnik				
Maßstab 1:1	Werkstoff	1.2312	Pos. Nr.	1
	Oberflächenrauheit Rz=25		Datum	März 2009
Allgemein-toleranzen mittel	Hochdruckwerkzeug Adapter		Name	Wilhelm H. Fischer C.

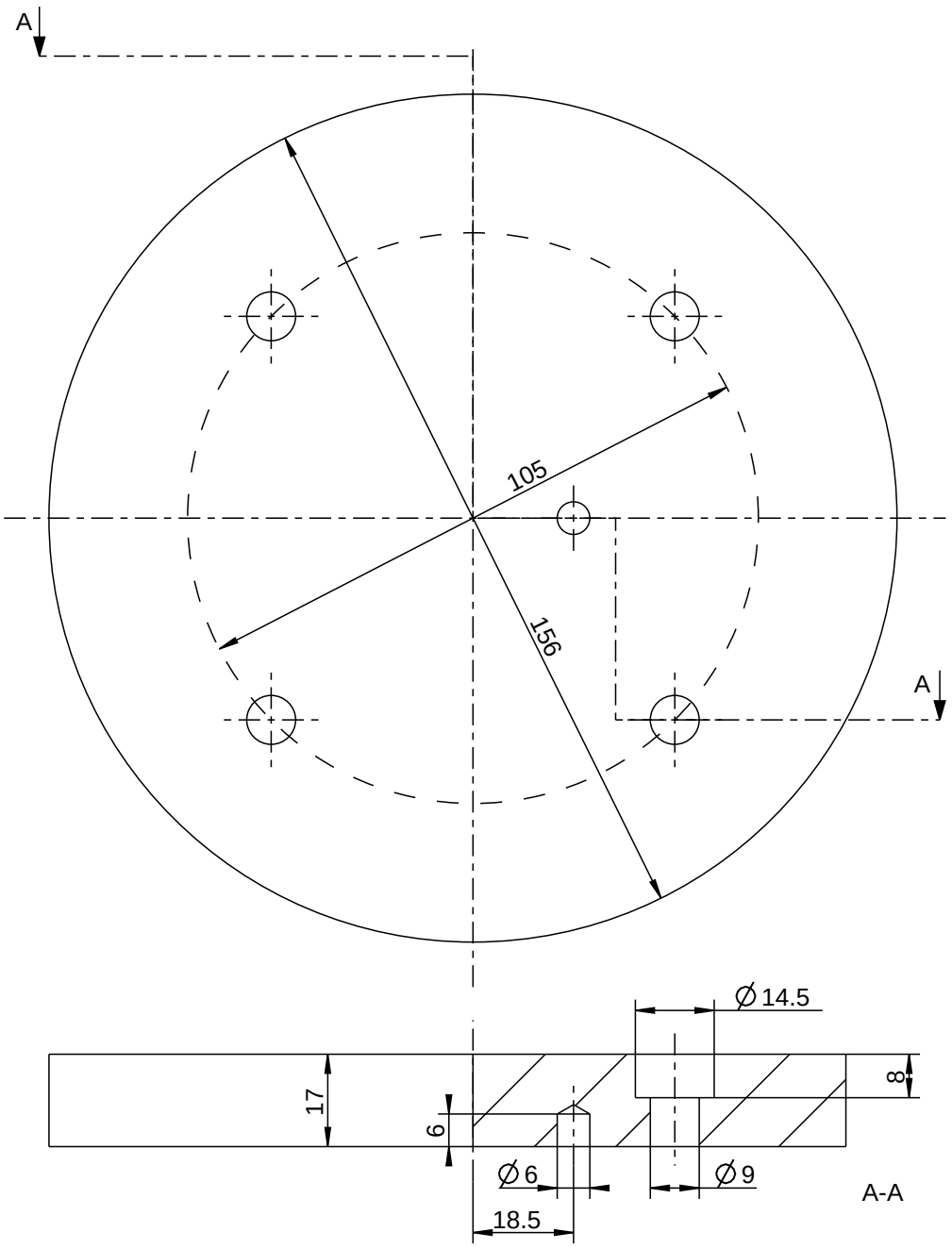

TGM Werkstoffingenieurwesen Kunststoff- und Umwelttechnik				
Maßstab 1:1	Werkstoff	1.1730	Pos. Nr.	20
	Oberflächenrauheit Rz=16		Datum	März 2009
Allgemein- toleranzen mittel	Hochdruckwerkzeug Aufspannplatte		Name	Wilhelm H. Fischer C.

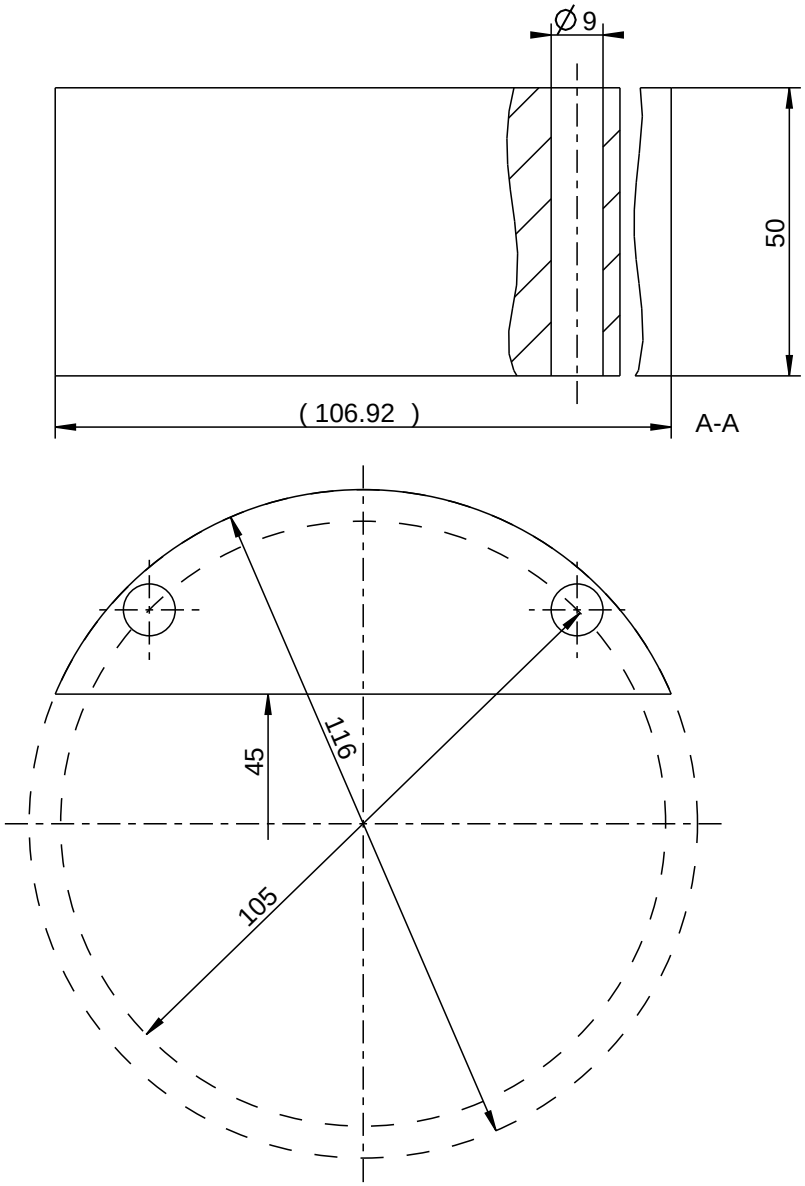

TGM Werkstoffingenieurwesen Kunststoff- und Umwelttechnik				
Maßstab 1:1	Werkstoff	1.1730	Pos. Nr.	8
			Datum	März 2009
Allgemein- toleranzen mittel	Hochdruckwerkzeug Distanzleiste		Name	Wilhelm H. Fischer C.

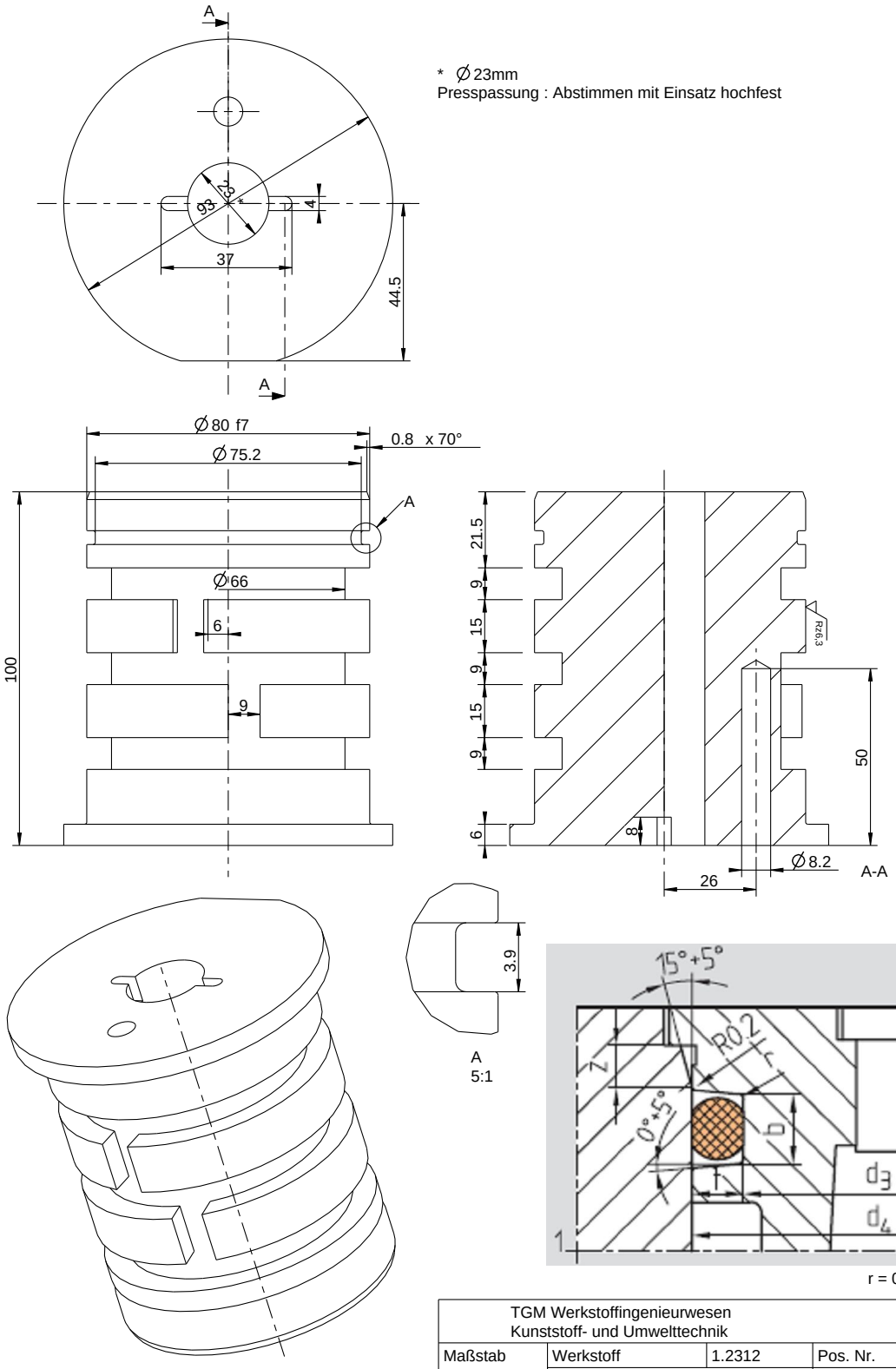

Ø 80 f7	79,970	79,940
Toleranz	Höchstmaß	Mindestmaß

TGM Werkstoffingenieurwesen Kunststoff- und Umwelttechnik				
Maßstab 1:1	Werkstoff	1.2312	Pos. Nr.	6
	Oberflächenrauheit Rz=25		Datum	März 2009
Allgemeintoleranzen mittel	Hochdruckwerkzeug Einsatz		Name	Wilhelm H. Fischer C.

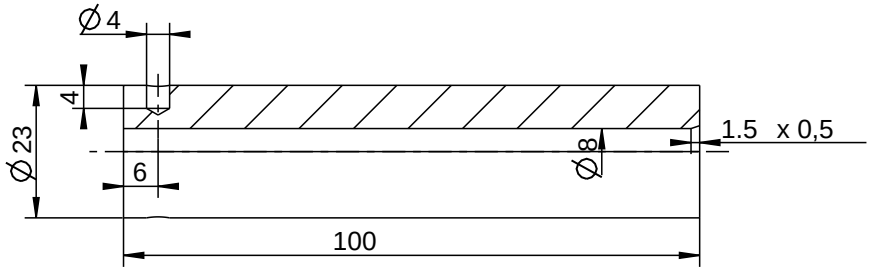

TGM Werkstoffingenieurwesen Kunststoff- und Umwelttechnik				
Maßstab 1:1	Werkstoff	1.2709	Pos. Nr.	11
	Oberflächenrauheit Rz=25		Datum	März 2009
Allgemein- toleranzen mittel	Hochdruckwerkzeug Einsatz hochfest		Name	Wilhelm H. Fischer C.

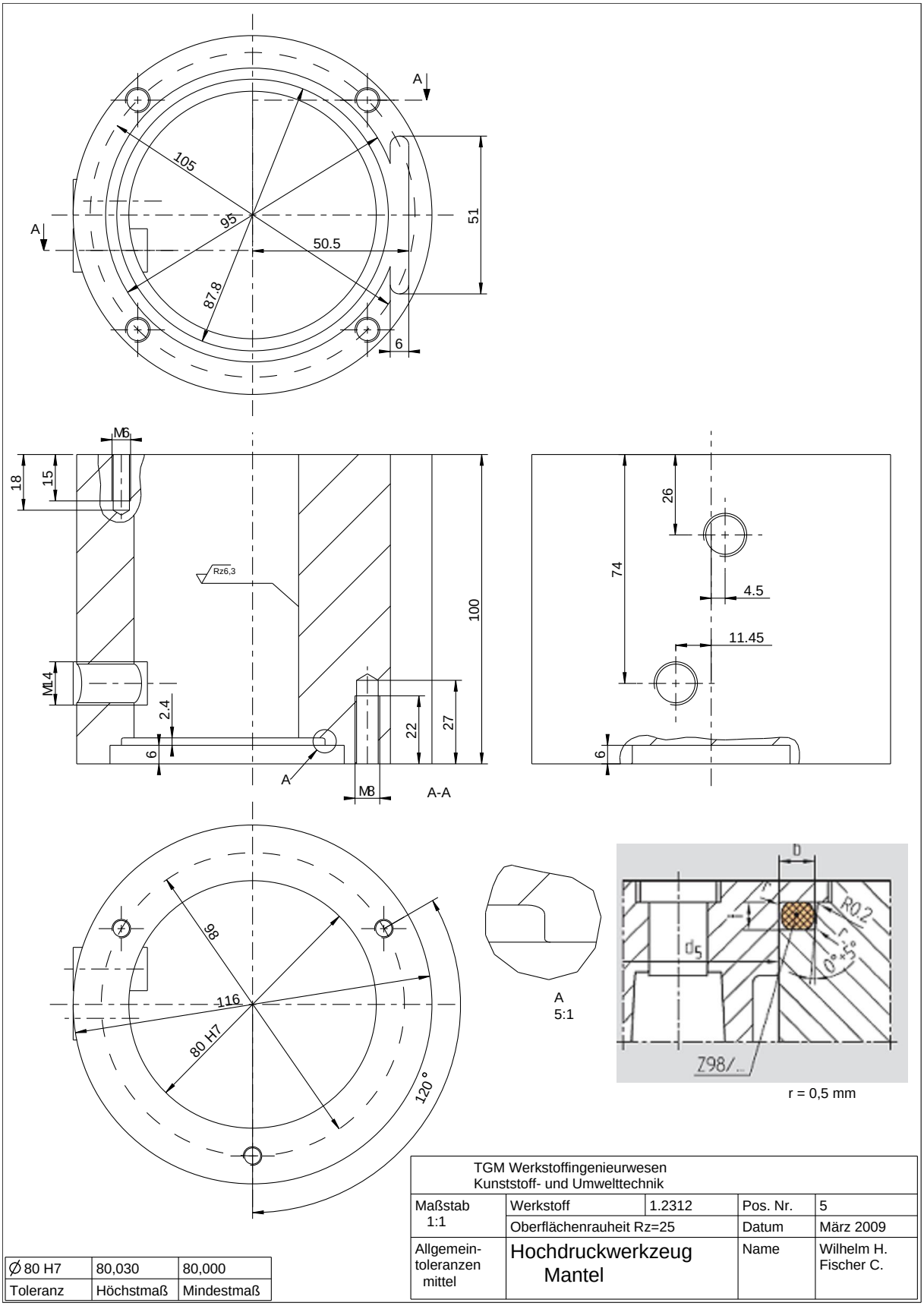

∅ 80 H7	80,030	80,000
Toleranz	Höchstmaß	Mindestmaß

TGM Werkstoffingenieurwesen Kunststoff- und Umwelttechnik				
Maßstab 1:1	Werkstoff	1.2312	Pos. Nr.	5
	Oberflächenrauheit Rz=25		Datum	März 2009
Allgemeintoleranzen mittel	Hochdruckwerkzeug Mantel		Name	Wilhelm H. Fischer C.

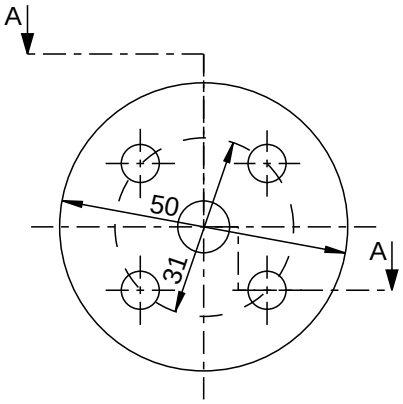

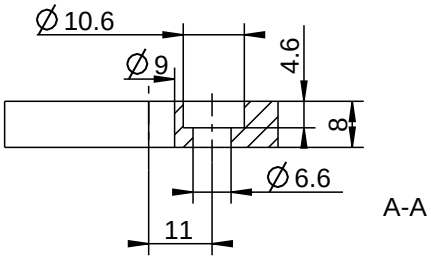

TGM Werkstoffingenieurwesen Kunststoff- und Umwelttechnik				
Maßstab 1:1	Werkstoff	1.2312	Pos. Nr.	3
	Oberflächenrauheit Rz=25		Datum	März 2009
Allgemeintoleranzen mittel	Hochdruckwerkzeug Rückhalteplatte		Name	Wilhelm H. Fischer C.

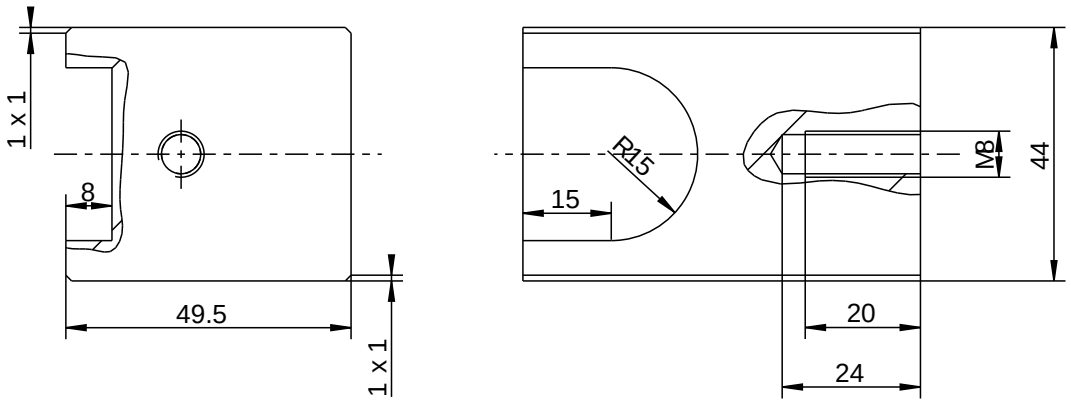

TGM Werkstoffingenieurwesen Kunststoff- und Umwelttechnik				
Maßstab 1:1	Werkstoff	1.1730	Pos. Nr.	18
	Oberflächenrauheit Rz=16		Datum	März 2009
Allgemein- toleranzen mittel	Hochdruckwerkzeug Schubelement		Name	Wilhelm H. Fischer C.

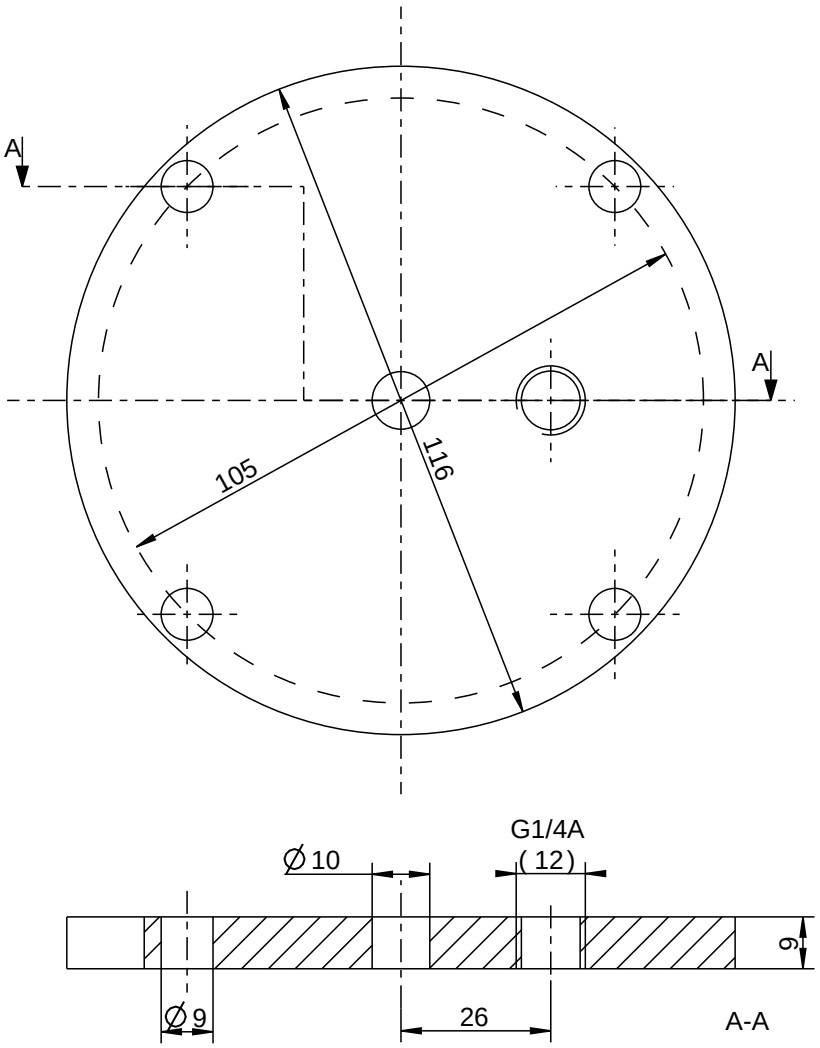

TGM Werkstoffingenieurwesen Kunststoff- und Umwelttechnik				
Maßstab 1:1	Werkstoff	1.1730	Pos. Nr.	24
	Oberflächenrauheit Rz=16		Datum	März 2009
Allgemein-toleranzen mittel	Hochdruckwerkzeug Stützplatte		Name	Wilhelm H. Fischer C.

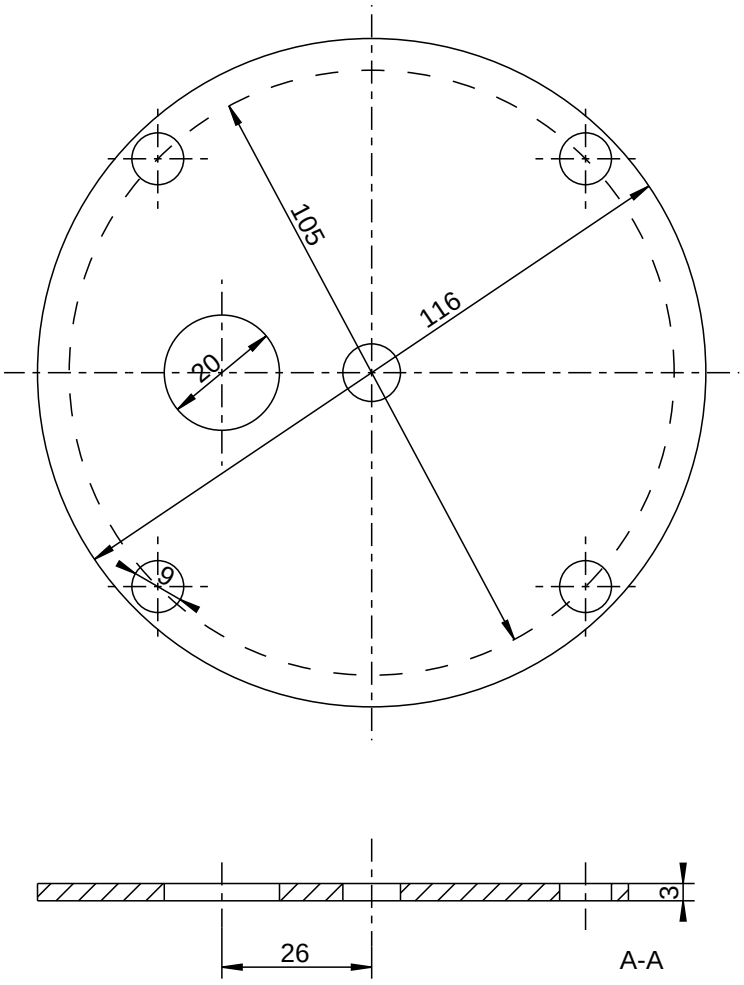

TGM Werkstoffingenieurwesen Kunststoff- und Umwelttechnik				
Maßstab 1:1	Werkstoff	Kunstharz	Pos. Nr.	7
			Datum	März 2009
Allgemein- toleranzen mittel	Hochdruckwerkzeug Wärmedämmplatte		Name	Wilhelm H. Fischer C.

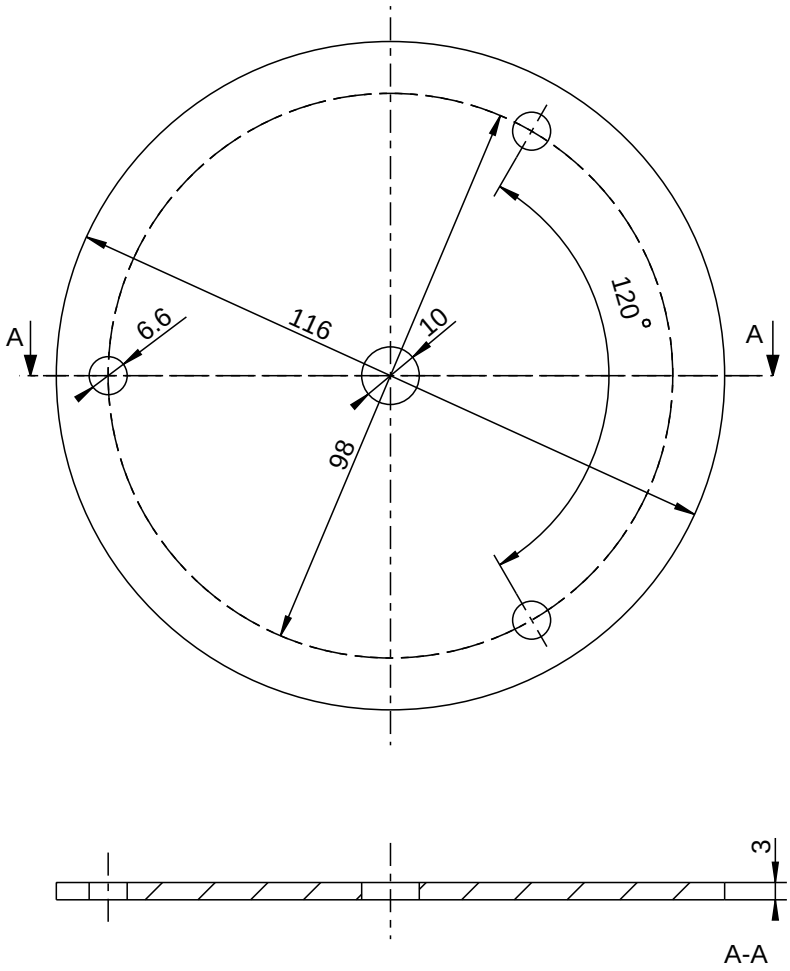

TGM Werkstoffingenieurwesen Kunststoff- und Umwelttechnik				
Maßstab 1:1	Werkstoff	Kunstharz	Pos. Nr.	4
			Datum	März 2009
Allgemein-toleranzen mittel	Hochdruckwerkzeug Wärmedämmplatte		Name	Wilhelm H. Fischer C.

02.10.2008 Ed.9

Polypropylene
HD120MO

Description
HD120MO is a polypropylene homopolymer with a good combination of mechanical properties intended for injection moulding.

Applications

Sanitary equipment
Caps and closures
General packaging

Physical Properties

Property	Typical Value Data should not be used for specification work	Test Method
Density	908 kg/m3	ISO 1183
Melt Flow Rate (230 °C/2,16 kg)	8 g/10min	ISO 1133
Tensile Modulus (1 mm/min)	1.500 MPa	ISO 527-2
Tensile Strain at Yield (50 mm/min)	9 %	ISO 527-2
Tensile Stress at Yield (50 mm/min)	33,5 MPa	ISO 527-2
Heat Deflection Temperature (0,45 N/mm²) [1]	88 °C	ISO 75-2
Charpy Impact Strength, notched (23 °C)	4 kJ/m²	ISO 179/1eA
Hardness, Rockwell (R-scale)	98	ISO 2039-2

[1] Measured on injection moulded specimens acc. to ISO 1873-2

Processing Techniques
This product is easy to process with standard injection moulding machines.

Following parameters should be used as guidelines:

Melt temperature	230 - 260 °C	
Holding pressure	200 - 500 bar	Minimum to avoid sink marks.
Mould temperature	10 - 30 °C	
Injection speed	As high as possible.	

Shrinkage 1 - 2 %, depending on wall thickness and moulding parameters

Storage
HD120MO should be stored in dry conditions at temperatures below 50°C and protected from UV-light. Improper storage can initiate degradation, which results in odour generation and colour changes and can have negative effects on the physical properties of this product.

Borealis AG | Wagramerstrasse 17-19 | 1220 Vienna | Austria
Telephone +43 1 224 00 0 | Fax +43 1 22 400 333
FN 269858a | CCC Commercial Court of Vienna | Website www.borealisgroup.com

BOREALIS

8. Cirriculum Vitae

Gerald Polt

born	March 1, 1984
in	Eisenstadt, Austria
marital status	unmarried
nationality	austrian

Education

since 2005	Studies –Physics, University of Vienna, Austria Diploma thesis: **“ Mechanisms of plastic deformation in γ-isotactic Polypropylene”**
2004	Austrian Matura (A-levels) at Secondary College for Mechanical Engineering- Special Training Focus Aeronautical Engineering, Eisenstadt, Austria
1998	Secondary College for Mechanical Engineering- Special Training Focus Aeronautical Engineering, Eisenstadt, Austria
1994	Bundesrealgymnasium (high school), Eisenstadt, Austria
1990	Volksschule St. Margarethen (elementary school), St. Margarethen, Austria

Talks

September 2010: **"Mechanisms of Plasticity in γ-Polypropylene"**
International Conference on Polymer Behavior ICPB,
Lodz, Poland

Publications

Determination of Lamella Thickness Distributions in Isotactic Polypropylene by Xray Line Profile Analysis, F. Spieckermann, H. Wilhelm, M. Kerber, E. Schafler, G. Polt, S. Bernstorff, F. Addiego and M.J. Zehetbauer, Polymer 2010, 51(18), 4195.

The role of dislocations for the plastic deformation of semicrystalline polymers as investigated by multi-reflection X-ray line profile analysis, F. Spieckermann, G. Polt, H.Wilhelm, M. Kerber, E. Schafler, M.J. Zehetbauer, submitted to Journal of Applied Polymer Science

List of Abbreviations

T_m	melting temperature
CRSS	critical resolved shear stress
CSD	Coherently Scattering Domain Size
FWHM	Full Width at Half Maximum
iPP	isotactic Polypropylene
MXPA	Multireflexion X-ray Profile Analysis
PE	Polyethylene
SAXS	Short Angle X-ray Scattering
WAXS	Wide angle X-ray scattering

Bibliography

[1] R Séguéla. Plasticity of semi-crystalline polymers : crystal slip versus melting-recrystallization. *e-polymers*, page 032, 2007.

[2] H. Wilhelm, A. Paris, E. Schafler, S. Bernstorff, J. Bonarski, T. Ungar, and M.J. Zehetbauer. Evidence of dislocations in melt-crystallised and plastically deformed polypropylene. *Materials Science and Engineering A*, 387-389:1018–1022, 2004.

[3] I.C. Dragomir and T. Ungar. Contrast factors of dislocations in the hexagonal crystal system. *J. Appl. Crystallogr.*, 35(5):556–564, 2002.

[4] T. Ungár, J. Gubicza, G. Ribárik, and A. Borbély. Crystallite size distribution and dislocation structure determined by diffraction profile analysis: principles and practical application to cubic and hexagonal crystals. *J. Appl. Crystallogr.*, 34(3):298–310, Jun 2001.

[5] Tacticity. [online image] available http://plc.cwru.edu/tutorial/enhanced/files/polymers/struct/struct.htm, October 7 2010.

[6] G. W. Ehrenstein. *Polymer-Werkstoffe: Struktur – Eigenschaften – Anwendung.* Carl Hanser Verlag München Wien, 1999.

[7] Spherulites. [online image] available. http://www.tufts.edu/∼pcebe/polymer_spherulites_2006.jpg, September 28 2010.

[8] L. Lin and A. S. Argon. Structure and plastic deformation of polyethylene. *J. Mater. Sci.*, 29(2):294–323, January 1994.

[9] Structure. [online image] available. http://www.princeton.edu/∼polymer/fig4.gif, December 22 2010.

[10] B. Lotz, J. C. Wittmann, and A. J. Lovinger. Structure and morphology of poly-(propylenes): a molecular analysis. *Polymer*, 37(22):4979–4992, October 1996.

[11] K. Mezghani and P. J. Phillips. The [gamma]-phase of high molecular weight isotactic polypropylene. ii: The morphology of the [gamma]-form crystallized at 200 mpa. *Polymer*, 38(23):5725–5733, November 1997.

[12] R. Krache, R. Benavente, J. M. Lopez-Majada, J. M. Perena, M. L. Cerrada, and E. Perez. Competition between α, β, and γ polymorphs in a β-nucleated metallocenic isotactic polypropylene. *Macromolecules*, 40(19):6871–6878, September 2007.

[13] E. Lezak, Z. Bartczak, and A. Galeski. Plastic deformation of the γ phase in isotactic polypropylene in plane-strain compression. *Macromolecules*, 39(14):4811–4819, July 2006.

[14] R. Thomann, C. Wang, J. Kressler, and R. Mulhaupt. On the gamma-phase of isotactic polypropylene. *Macromolecules*, 29(26):8425–8434, 1996.

[15] Stefano V. Meille, S. Bruckner, and W. Porzio. γ-isotactic polypropylene. a structure with nonparallel chain axes. *Macromolecules*, 23(18):4114–4121, September 1990.

[16] B. Lotz, S. Graff, C. Straupé, and J.C. Wittmann. Single crystals of [gamma] phase isotactic polypropylene: combined diffraction and morphological support for a structure with nonparallel chains. *Polymer*, 32(16):2902 – 2910, 1991.

[17] D.R. Norton and A. Keller. The spherulitic and lamellar morphology of melt-crystallized isotactic polypropylene. *Polymer*, 26(5):704 – 716, 1985.

[18] A Turner-Jones. Development of the [gamma]-crystal form in random copolymers of propylene and their analysis by dsc and x-ray methods. *Polymer*, 12(8):487–508, August 1971.

[19] Khaled Mezghani and Paul J. Phillips. [gamma]-phase in propylene copolymers at atmospheric pressure. *Polymer*, 36(12):2407–2411, 1995.

[20] K. Mezghani and P. J. Phillips. The [gamma]-phase of high molecular weight isotactic polypropylene: Iii. the equilibrium melting point and the phase diagram. *Polymer*, 39(16):3735–3744, July 1998.

[21] G. Gottstein. *Physical Foundations of Material Science*. Springer-Verlag Berlin Heidelberg, 2004.

[22] Hein-Peter Stüwe. *Einführung in die Werkstoffkunde*. Bibliographisches Institut & F.A. Brockhaus AG, 1991.

[23] Screw and edge dislocations in a crystal. [online image] available. http://courses.eas.ualberta.ca/eas421/lecturepages/microstructurediags.html♯bergers, September 28 2010.

[24] Dislocation line. [online image] available. http://oregonstate.edu/instruct/engr322/Exams/Previous/S98/ENGR322MT2.html, October 14 2010.

[25] L. G. Shadrake and F. Guiu. Dislocations in polyethylene crystals: line energies and deformation modes. *Philos. Mag.*, 34(4):565–581, 1976.

[26] G.H. Michler. *Kunststoff Mikromechanik*. Carl Hanser Verlag München Wien, 1992.

[27] X–ray tube. [online image] available. http://pubs.usgs.gov/of/2001/of01-041/htmldocs/images/xrdtube.jpg, September 28 2010.

[28] Ryong-Joon Roe. *Methods of X-ray and Neutron Scattering in Polymer Science*. Oxford University Press, 2000.

[29] F.J. Balta-Calleja and C.G. Vonk. *X-Ray Scattering of Synthetic Polymers*. Elsevier, 1989.

[30] Bremsstrahlung. [online image] available. http://www4.nau.edu/microanalysis/Microprobe-SEM/Images/Bremsstrahlung.jpg, September 28 2010.

[31] Radiation. [online image] available. http://www.roentgenanalytik.de/images/4koepfede/Entstehung_RF–Strahlung_de.jpg, September 28 2010.

[32] Radiation spectrum. [online image] available. http://www.xtal.iqfr.csic.es/Cristalografia/archivos_02/sierra.gif, September 28 2010.

[33] Atomic waves. [online image] available. http://de.academic.ru/dic.nsf/dewiki/193906, September 28 2010.

[34] Interference. [online image] available. http://de.academic.ru/dic.nsf/dewiki/193906, September 28 2010.

[35] Bragg reflection. [online image] available. http://www.microscopy.ethz.ch/bragg.htm, September 28 2010.

[36] G. K. Williamson and W. H. Hall. X-ray line broadening from filed aluminium and wolfram. *Acta Metallurgica*, 1(1):22–31, January 1953.

[37] T. Ungár and A. Borbély. The effect of dislocation contrast on x-ray line broadening: A new approach to line profile analysis. *Appl. Phys. Lett.*, 69(21):3173–3175, 1996.

[38] Florian Spieckermann. *Investigation of Deformation Induced Changes of the Microstructure of Semicrystalline Polymers and their Impact on Mechanical Properties*. PhD thesis, University of Vienna, 2010.

[39] B. E. Warren and B. L. Averbach. The effect of cold-work distortion on x-ray patterns. *J. Appl. Phys.*, 21(6):595–599, June 1950.

[40] B. E. Warren and B. L. Averbach. The separation of cold-work distortion and particle size broadening in x-ray patterns. *J. Appl. Phys.*, 23(4):497–497, April 1952.

[41] M. A. Krivoglaz. Theory of x-ray and thermal neutron scattering by real crystals. *Plenum Press New York*, 1969.

[42] M. Wilkens. The determination of density and distribution of dislocations in deformed single crystals from broadened x-ray diffraction profiles. *Physica Status Solidi (a)*, 2(2):359–370, 1970.

[43] T. Ungar and G. Tichy. The effect of dislocation contrast on x-ray line profiles in untextured polycrystals. *Physica Status Solidi (a)*, 171(2):425–434, 1999.

[44] G. Ribárik, T. Ungár, and J. Gubicza. *MWP-fit*: a program for multiple whole-profile fitting of diffraction peak profiles by *ab initio* theoretical functions. *J. Appl. Crystallogr.*, 34(5):669–676, Oct 2001.

[45] Gabor Ribarik. *Modelling of diffraction patterns based on microstructural properties*. PhD thesis, Eötvös Lorand University, 2008.

[46] T. Ungar. The meaning of size obtained from broadened x-ray diffraction peaks. *Adv. Eng. Mater.*, 5(5):323–329, 2003.

[47] T. Ungar. Microstructural parameters from x-ray diffraction peak broadening. *Scripta Materialia*, 51(8 SPEC. ISS.):777–781, 2004.

[48] H. Wilhelm. Phd thesis, university of vienna, in progress. unpublished results.

[49] M. Kerber. Phd thesis, university of vienna, in progress. unpublished results.

[50] D. Breuer, P. Klimanek, and W. Pantleon. X-ray determination of dislocation density and arrangement in plastically deformed copper. *J. Appl. Crystallogr.*, 33(5):1284–1294, Oct 2000.